IDA

Luminescent Spectral Splitting: Efficient Spatial Division of Solar Spectrum at Low Concentration for Multijunction Photovoltaic Modules

Brent Fisher
John Biddle

The Institute for Defense Analyses is a non-profit corporation that operates three federally funded research and development centers to provide objective analyses of national security issues, particularly those requiring scientific and technical expertise, and conduct related research on other national challenges.

INSTITUTE FOR DEFENSE ANALYSES

IDA Paper NS P-4659

Luminescent Spectral Splitting: Efficient Spatial Division of Solar Spectrum at Low Concentration for Multijunction Photovoltaic Modules

Brent Fisher
John Biddle

Executive Summary

The purpose of this study was to investigate the potential performance of a novel concept for dividing solar radiation into spectral components that separately illuminate photovoltaic (PV) cells of different bandgaps using an optical design that (1) is simple, easily manufactured, and extensible to many spectral channels, and (2) does not achieve high geometric concentration factors. The concept that we explore leverages the approach of stacked luminescent solar concentrators (LSCs) for dividing the solar spectrum using fluorophores that are tuned to different spectral bands. However, whereas multicolor LSCs must perform two functions using the same optical component—spectral division and concentration—we consider the performance of a similar design when only one demand—spectral division—is placed on it. We find that the optical quantum and power efficiencies can be quite high (QE > 90%, PE > 80%) compared to what one might intuitively expect. When we couple the light output to a simple detailed balance model of a solar cells using experimental performance parameters we find that solar-to-electric conversion could exceed 30% with four junctions, using existing PV materials. While this does not exceed what can be achieved by HCPV designs on multijunction epitaxially grown stacks, the concept presented here has the major advantage of being easily extensible to an arbitrarily large number of spectral channels. Because of this extensibility, the number of junctions in the system is limited only by the availability of PV cells with appropriate bandgaps, so significantly higher system efficiencies should be accessible without major revision to the basic design presented here.

CONTENTS

1. Introduction

Optical division of the solar spectrum, known as "spectral splitting," is an old concept that enables designing a multijunction PV module with a number of potential advantages: (1) current matching all the subcells is not required; (2) each subcell material may be fabricated on a different substrate, so there is no need for lattice matching or thick metamorphic layers, and each subcell may be independently optimized; (3) a larger number of junctions may be accessible. Concepts for spectral splitting have generally always considered spectral splitting in combination with optical concentration, but combining these functions into a single design can lead to problems. Designs based on dichroics are fundamentally challenged because concentration leads to large distributions of input angles, but the performance of dichroics for spectral splitting degrades when the range of angles it must accommodate becomes large. Stacks of luminescent solar concentrators (LSCs) are another option for spectral division and concentration, but their optical efficiency has been severely constrained by reabsorption within the devices.

In this paper we consider a concept that aims to split the solar spectrum with maximum optical efficiency, but using a simple design that is easy to manufacture and is easily extensible to an arbitrary number of subcells. Optical concentration is used in this design, but high concentration is not a requirement. Dispensing with high concentration as the singular focus permits us to explore a design space of what we call luminescent spectrum splitters (LSS), which are essentially a variation on LSCs that focuses first on high efficiency and good spectral splitting, with concentration a secondary concern. Based on a home-built ray-tracing simulation that uses experimental data to model the performance of luminescent materials, optical quantum efficiencies of 95% are achievable with optical power efficiencies of 75% (after the Stokes shift of the emission). An extension of this model couples the optical output to PV materials reported in literature and suggests that module efficiencies of 30%–35% and higher could be realized by these designs. A very clear trade-off between net optical concentration and efficiency is explored, and a few design variations that could overcome this tradeoff are discussed. Because we find that high-efficiency operation is currently limited to designs with fairly low concentration (<10×), this approach may not be economically viable if the PV materials are high cost (e.g., III-V materials). However, this work demonstrates that if a fairly low-cost PV were available at a wide variety of bandgap values, the LSS concept could provide a highly efficient, manufacturable, and easily extensible approach to a stitching the PV materials together in a multijunction module.

2. Background

It is well known that solar-to-electric conversion efficiency can be greatly enhanced by using more than one bandgap in a multijunction photovoltaic systen. The benefit is derived by breaking the tradeoff between high current and voltage that is the basis of the Shockley-Quiesser limit. The great majority of multijunction PV devices in both research and production are based on multiple junctions stacked in optical series, usually by epitaxial growth of one material on another. An alternative approach to the multijunction stack is to employ optics that separate portions of the incident solar spectrum and direct them to different spatial locations. This concept has been around for many decades, and a thorough review is given by Imenes and Mills [1]. Some examples of efforts to optically split the solar spectrum include the RAINBOW multijunction design from NASA [2, 3], holographic splitting [4], and more recently a DARPA-funded CPV project [5, 6]. There are at least two potential advantages associated with optical separation of the solar spectrum:

1. The individual PV cells do not need to be epitaxially grown on top of one another, so the material choices and growth conditions are less restricted. In principle each junction could be grown on a separate substrate. This would of course multiply substrate costs, but it would also reduce growth time and precursor usage often associated with graded layers in metamorphic devices or many of the other intermediate layers (e.g., tunnel junctions) required in complex multijunctions.
2. Each individual junction may be separately contacted without the need for transparent, buried contacts so there is no current matching requirement across the PV devices. Among other things such a device would be less susceptible to diurnal and seasonal variation of the illumination spectrum—a problem that limits the practical efficiency gains of series connected multijunction devices when the number of junctions becomes large [7].

A variety of optical designs have been proposed and built for the purpose of spatially dividing the solar (or any broadband) spectrum. Most of these employ either dispersion in an optical material (e.g., a prism) or a wavelength-dependent reflective surfaces such as dichroic mirrors. There are at least three aspects of designs based on dichroic mirrors that are not ideal. First, the wavelength at which a dichroic mirror switches from reflective to transmissive depends on the angle of incidence of the propagating light. This means that if the light field incident on the dichroic is composed of rays incident over a wide distribution of angles (as found at the output of a primary concentrating optic), then each ray will encounter a dichroic with a different cutoff wavelength. A weighted average of the dichroics reflectance spectrum over all these

angles can yield spectral division that is not very sharp. A second challenge associated with optical designs based on dichroics is their "extensibility." A design might be found that performs well for separation of the spectrum into two components, but adding third, fourth, or fifth channel would usually require a complete redesign. The third challenge associated with optical designs based on dichroics and assembled from many individual pieces is economic cost. High-performance dichroics can easily cost many hundred dollars per square meter, and the manufacturing of assemblies with large part counts drives up cost.

Stacked LSCs offer an alternative to dichroics for spectrum splitting, but these generally have not yielded high optical efficiencies. The major challenge associated with LSCs is reabsorption of the wave-guided photons before they are able to reach the targeted PV cells. The degree to which reabsorption limits the performance of an LSC is directly connected to its geometric dimensions [8] (aspect ratio) which is, by definition, its concentration factor. In short, it is the demand for *both* concentration and spectrum splitting functionality that makes high-efficiency LSCs difficult to realize. The concept we present here dispenses with large net concentration as a requirement to explore how high the optical and system efficiency of a luminescent spectrum splitter (LSS) can be with concentration of secondary importance in the design requirements.
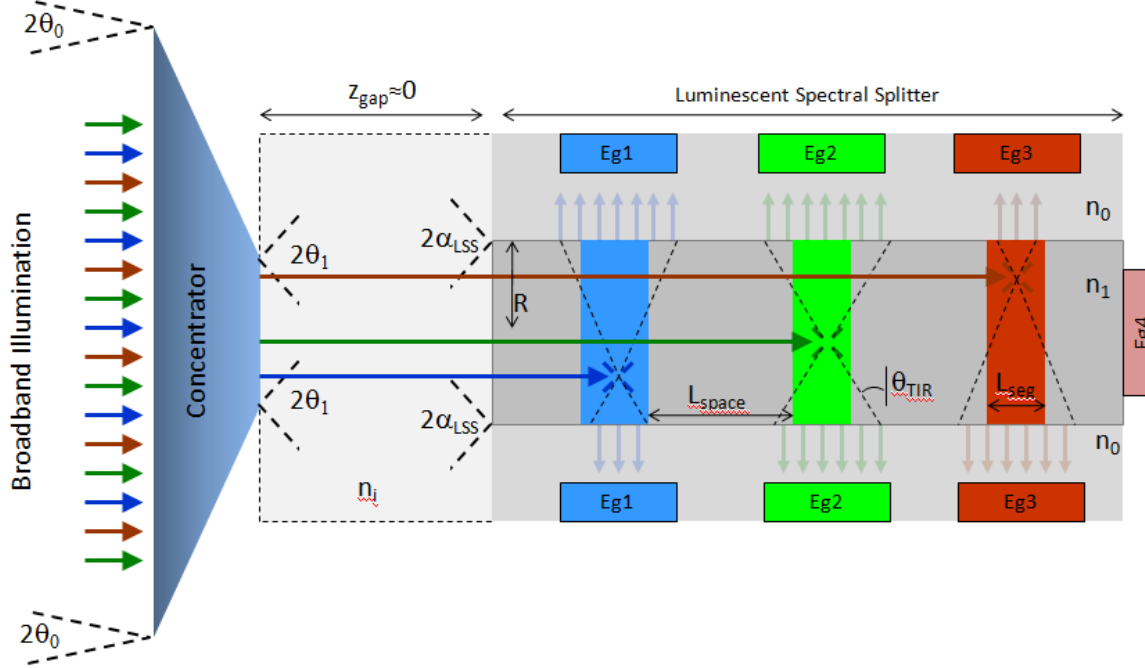
3. Concept

Figure 1 is an illustration of the particular instantiation of our concept. The first component is an unspecified non-imaging concentrator optic such as a compound parabolic concentrator. The second component is simply a cylindrical light guide through which light propagated by total internal reflection (TIR). The function of splitting the spectrum is fulfilled in the lightguide by doping sequential segments of it with a tunable fluorophore that has a very high luminescent quantum yield, in this case semiconductor nanocrystals. The technology for embedding semiconductor nanocrystals inside polymer matrices or inorganic matrices with little loss of luminescent quantum yield (QY) has been previously established by various routes ranging from polymerization [9–12] to sol-gel composites [13–15], so the manufacture of such optical components is certainly possible. The principle of operation is evident from the figure: broadband, plane-wave light is incident on the primary optic and concentrated before entering the second component where each wavelength propagates until it encounters a segment that is doped with nanocrystals whose bandgap is lower in energy than the given wavelength. Photons that are absorbed by the fluorophores are then re-emitted isotropically. Some photons will be captured within the waveguide, propagating back out the entrance aperture of the device—these are lost. Others may propagate further down the device to be absorbed by the next color segment, while the rest will not meet the TIR condition and will exit the waveguide laterally. It is along these color segments where PV materials would be placed to collect the narrowband radiation that is emitted from each color segment of this luminescent spectrum splitter (LSS). For our investigation we primarily considered a cylindrical design with rotational symmetry about the z-axis, but rectilinear or other designs are also possible. More detailed investigations could compare performance of these categories.

A. Parameters

Before undertaking a detailed analysis of this concept, we identified the relevant design parameters and investigated the tradeoffs required between these. These parameters, illustrated in Figure 1, are the following:

n_0	Refractive index of cladding on LSS
n_1	Refractive index of LSS interior
n_i	Refractive index at input to LSS and exit of primary optic
L_{seg}/R	Unitless ratio between length of color segment and radius of rotationally symmetric LSS

Figure 1. Diagram of luminescent spectral splitting concept (not to scale). The gap between primary concentrator and the LSS is inflated so that angle definitions can be illustrated.

P_{trans}	Probability of transmission for a photon traveling parallel to the z-axis when it encounters a color segment and has a wavelength equal to the band-edge absorption peak of the nanocrystal dopants.
L_{space} / R	Unitless ratio of the length of spacing between color segments and the radius of the rotationally symmetric LSS
θ_{in}	Acceptance half angle of primary concentrator. For calculation of maximum primary concentration we assume that $\theta_{in} = 1.5$ deg.

These design parameters can be used to immediately compute a few key quantities that describe a design's performance. The TIR angle θ_{TIR} is the angle of incidence inside the waveguide at which TIR kicks in—the larger the TIR angle, the more likely an isotropically emitted photon will exit the waveguide.

$$\theta_{TIR} = \sin^{-1}(n_0/n_1) \tag{1}$$

The acceptance angle of the LSS, α_{LSS}, on the other hand is the maximum angle for which TIR will be supported within the light guide. Photons that are incident at angles greater than α_{LSS} do not propagate through the LSS.

$$\alpha_{LSS} = \sin^{-1}\left(\sqrt{n_1^2 - n_0^2}/n_i\right) \tag{2}$$

6

If we demand that the range of angles at the output of the primary optic is contained within the acceptance angle of the LSS, the maximum concentration permitted by 100% conservation of optical etendue is given by (see reference [16]):

$$C_{1max} = \left(\frac{n_{out}\sin(\theta_{out})}{n_{in}\sin(\theta_{in})}\right)^2 = \left(\frac{n_i\sin(\alpha_{LSS})}{1\times\sin(\theta_0)}\right)^2 = \left(\frac{n_1^2-n_0^2}{\sin^2(\theta_0)}\right) \tag{3}$$

Finally, the degree to which the LSS de-concentrates input radiation is just the ratio between the area of the cylinder wall that the PV material must cover to capture any photons emitted from a given color segment and the area of the input aperture of the LSS:

$$D_{max} = \frac{2\pi R(L_{seg}+L_{space})}{\pi R^2} = \frac{2L_{seg}}{R}\left(1 + \frac{2R\tan\theta_{TIR}}{L_{seg}}\right) \tag{4}$$

Where the first factor $2L_{seg}/R$ is the de-concentration resulting from covering the entire length of a color segment with PV, and the second factor, $(1 + 2R\tan\theta_{TIR} / L_{seg})$, is an approximation of how much extra coverage is needed to collect emitted photons with the steepest angle for which a meridional ray still does not meet TIR and can escape. In this expression the de-concentration D is given the subscript "max" because we measure the de-concentration according to the largest area over which photons might be spread according to not meeting the TIR condition. Also note that we assume L_{space}, the spacing between color segments, is set such that it is twice the maximum z distance a photon could traverse while still not meeting the TIR condition and exiting: $L_{space} = R \times \tan\theta_{TIR}$.

So the net concentration of the system is computed as,

$$C_{NET} = \left(\frac{n_1^2-n_0^2}{\sin^2(\theta_0)}\right)\bigg/\left(\frac{2L_{seg}}{R}\left(1 + \frac{2R\tan\theta_{TIR}}{L_{seg}}\right)\right) \tag{5}$$

Without any consideration of dopant fluorophores we can immediately recognize a fundamental tradeoff of this concept. As the difference between the cladding and core refractive indices decreases, the TIR angle increases and the fraction of isotropically emitted photons that can escape likewise increases. At the same time, however, the LSS acceptance angle α_{LSS} decreases, causing the maximum concentration permitted by the primary optic to decrease. There is a tradeoff between the fraction of isotropically emitted photons that are collected (exit through side) and the net concentration of the system. This is illustrated in Figure 2.

Another expected limitation on the concentration levels that would be practical in this device is a consequence of heating that occurs when the luminescent materials in the LSS absorb solar illumination and re-radiate at longer wavelengths. Any difference between the energy of the photon absorbed and the photon that is re-emitted is converted

to heat. The minimum amount of heating is the energy of the Stokes shift between the lowest energy photons that can be absorbed and the energy of the photons emitted.
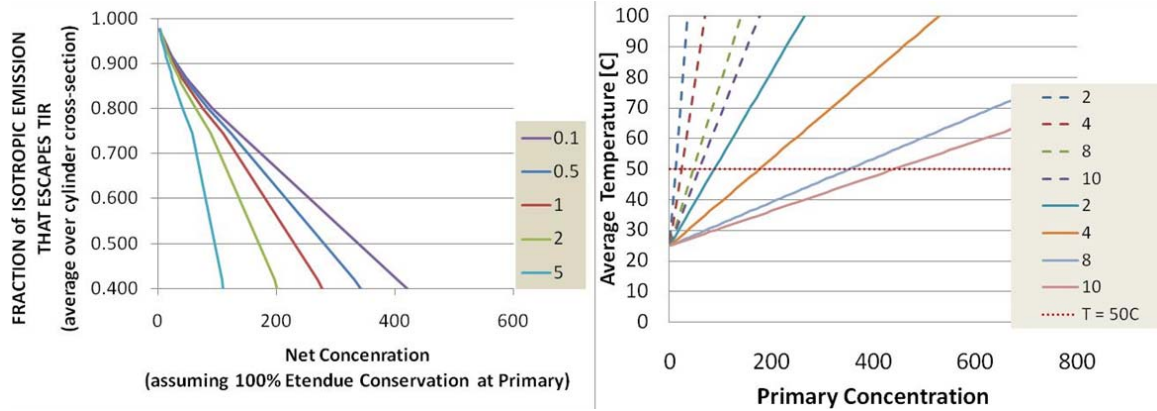
Figure 2. Expected limitations on concentration for the LSS concept. Left: the fraction of isotropic luminescence that can exit the LSS through the side (as calculated in Appendix B) is plotted against the C_{NET} (given in equation 5) by varying the cladding index n_0. Each line corresponds to a different value of L_{seg}/R. Right: estimates of the steady-state temperature in a disk as a function of concentration if 850 W/m^2 is incident and 80% of the incident light is converted to heat. Different lines indicate different L_{seg}/R aspect ratios of the "disks." Dashed lines assume a surface heat-transfer coefficient out the sides of the disk (excluding the top/bottom of disk) of h = 20 W/m^2/K. Solid lines assume h = 150 W/m^2/K.

If PV material and cell costs are a major component of the cost structure when designing an LSS, then the best design will strike a compromise between permitting high concentration while collecting reasonably high fractions of isotropic emission. Figure 2 shows, though, that the more one tries to drive up the concentration, the more collection efficiency will drop and the higher internal temperatures will be driven. On the other hand, if PV material costs are not overwhelming, the optimal design may drive photon collection fraction (i.e., QE) up while sacrificing net optical concentration. It is in this regime of low net concentration where our investigation of LSS will focus.

B. Experimental Methods

To investigate the performance of this optical system in more detail than is permitted by simple analytical expressions (with no approximations), we constructed a Monte Carlo ray-tracing model that simulates the propagation of incident photons through the LSS. In this model, rays are introduced to the inside of the LSS at uniformly random locations across the input aperture of the LSS. The initial propagation direction of each photon is randomly drawn from uniform distributions in *xy*-plane azimuth and from a user-defined distribution for the angle theta between the direction of propagation and the *z*-axis. For most runs the input theta distribution was uniform between 0 and α_{LSS}

8

and zero otherwise.[1] At each propagation step of the ray-tracing one of three possible events was possible: (1) absorption by a chromophore, (2) intersection with the sidewall of the LSS, or (3) intersection with the boundary between adjacent segments. For each of these three outcomes a distance is computed at each step: the distance to the sidewall, the distance until the z-plane of intersection between two segments is reached, and a randomly drawn absorption distance based on Beers law using an extinction coefficient obtained from the absorption spectra for the fluorophore found in the present segment. Whichever distance is shortest determines which event occurs at each propagation step. If case (3) occurs nothing is changed, and the photon continues on the same trajectory in the next step. If case (2) occurs—sidewall intersection—then the angle of incidence and associated Fresnel reflection coefficient are computed. A random number is drawn and compared with this reflection coefficient to determine whether or not the photon exits the LSS. If the photon is absorbed (case 1) then a random number is drawn and compared to the quantum yield of the chromophore to determine whether or not a new photon is re-emitted. If one is re-emitted its new propagation direction is obtained by random draw from uniform distributions of zenith and azimuth angles, and its new wavelength is obtained by random draw from a distribution set by the fluorophore's emission spectrum, modified such that the emission wavelength is not permitted to be smaller than the wavelength of the photon before it was absorbed. This simple approach to propagating photons through the LSS permits most of the relevant physics to be captured. Iteration over N photons allows the performance of the LSS to be simulated. For batch runs to investigate parameter dependencies we usually used $N = 20,000$, and for results presented here we used $N = 100,000$ photons to simulate the performance.

For our study we sought to simulate a system that is realistically feasible using present technology. We chose glass or polymer materials doped with semiconductor nanocrystals to serve as the luminescent segments of the LSS. We selected a refractive index for the LSS of $n_1 = 1.62$, corresponding to optical glass, but the cladding index, n_0, was a varied parameter. We did not adjust n_1 to account for the presence of (higher index) nanocrystals because the loading fractions were relatively small. To emulate actual nanocrystal optical behavior we used absorption and emission spectra obtained from literature reports on actual materials. One advantage of using semiconductor nanocrystals in the LSS is the tunability of their bandgap based on nanocrystal size. This property along with the use of just three different nanocrystal materials (CdSe, InAs, and PbSe) would allow almost any band gap to be obtained between 450 nm and 2000 nm. We could not obtain separate unique spectra for every possible band-gap value. Therefore, we obtained absorption and emission spectra from six separate reports, and translated the

---

[1]   We also simulated input angle distributions that were (1) a delta function at $\theta_{incidence} = 0$ (i.e., a uniform plane wave in the z-direction) and (2) a realistic distribution obtained from a parabolic concentrator. The performance was quite insensitive to the initial distribution of input angles.

nearest spectrum to match whatever bandgap value was desired in each segment of the LSS in a simulation run.[2] The six absorption spectra are shown in Figure 3. The output of each Monte Carlo ray-tracing run was a data structure that contained the propagation history and fate of each test ray. From these data we derived all the results given in the next section.
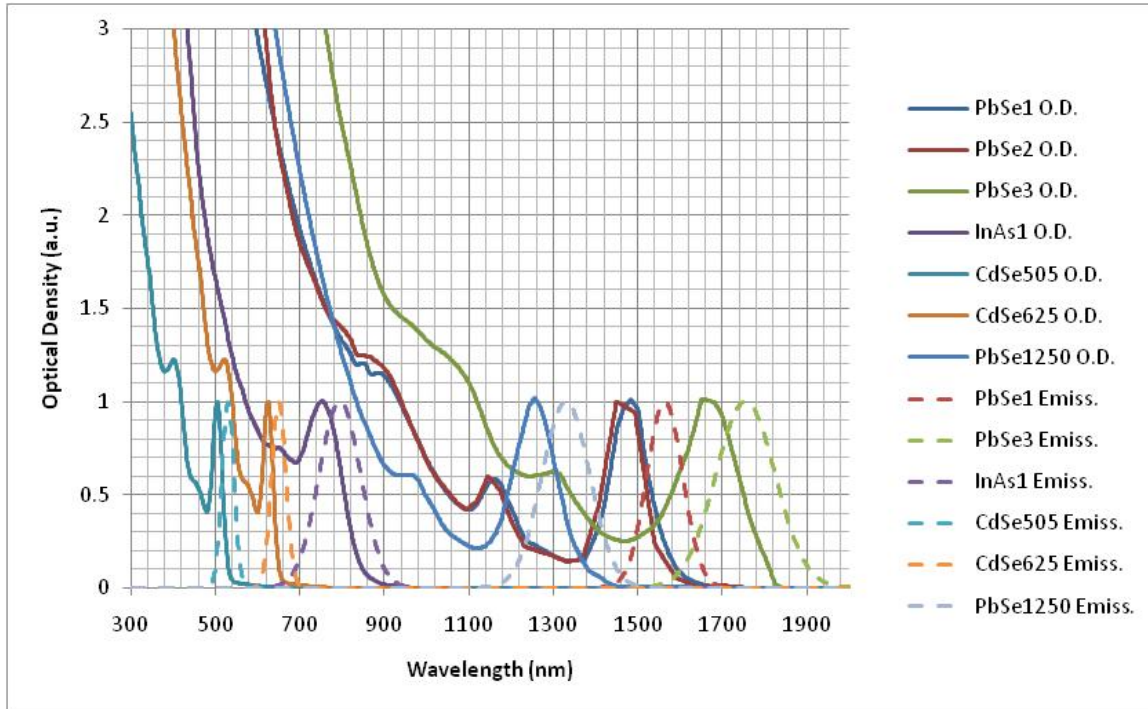
Figure 3. Absorption spectra used for model runs. Two of the spectra are from CdSe nanocrystals of different sizes [1, 2], one is from InAs nanocrystals [3], and the other three are from PbSe nanocrystals of various sizes [4–6].

---

[2] For example, if the spectrum for nanocrystals with a band edge absorption at 1600 nm were desired, the green spectrum in Figure 3 would be selected and translated such that its first absorption peak matched 1600 nm.

4. Results

Our simulation experiments had two main goals. First we sought to identify the design parameters that yielded the best optical efficiency for a given low optical concentration (2× to 10×). We then sought to quantify the sensitivity of the optical performance to these design parameters.

A. Quantum Efficiencies Attainable

To explore efficiency limits, we empirically optimized the optical efficiency by running batches of simulations in which we varied L_{seg}/R between 0.1 and 10, n_0 between 1.4 and 1.55, and P_{trans} between 0.0001 and 0.02, with other parameter values held constant ($n_1 = 1.62$, $QY = 1.0$). In general when L_{seg}/R increased and when n_0 increased, the optical efficiency increased (but concentration decreased). A number of parameter combinations were identified for which the optical quantum efficiency (QE, i.e., number of photons out divided by number input) exceeded 90%, and we present the results of one typical high QE example in this section.

When we set $L_{seg}/R = 5.0$ and $n_0 = 1.60$, we obtained QE = 94% and PE = 75% for the LSS (QE = 80% and PE = 70% when only side walls are counted). Figure 4 shows how the output spectrum varies along the length of the LSS when we assume an input concentration (C_1) of 94×. In this design, the spacing length is large enough ($L_{space}/L_{seg} = 5.0$) that the emission spectra from adjacent color segments do not overlap significantly. Furthermore, these data show that relatively narrowband emission exits each segment of the LSS. Based on the results of this run, the probability of reabsorption inside the same segment was 0.35, which gives a photon better than even odds of escaping without reabsorption. With some conversion[3] this reabsorption probability means that on average an emitted photon travels 2.3 times as far as the average distance to a boundary of the color segment before being reabsorbed [2.3 = –1/ln(1 – 0.35)]. For comparison, standard LSC designs have a ratio of average transmission length (l) to disk radius (r) in the range of $l/r = 0.05$ to 0.1. A good discussion of how l/r relates to re-absorption and overall efficiency of LSCs is given by Olson [8]. Because the QY was assumed to be 100% in these optimization simulations, the reabsorption did not have too severe an impact on the QE of the LSS. The most important source of QE loss by far was fluorescence. It traveled in the reverse direction back out the front (5%), which we term, "return losses." The

---

[3] From Beers law a simple derivation yields: $\bar{l}/\langle L(r,z,\phi,\theta)\rangle = -1/\langle \log(1 - p_{reabsorbtion})\rangle$ where $\langle ... \rangle$ indicates an average over r, z is the position from which a photon is emitted and ϕ, θ is the angular direction of its emission. $L(r,z,\phi,\theta)$ is the distance to the boundary of the color segment, and $\bar{l}$ is the inverse of the extinction coefficient (i.e., the average distance a photon propagates before being absorbed).

severity of this loss mode does depend on the how many cycles of re-emission a ray undergoes, but for this design it was not too severe.
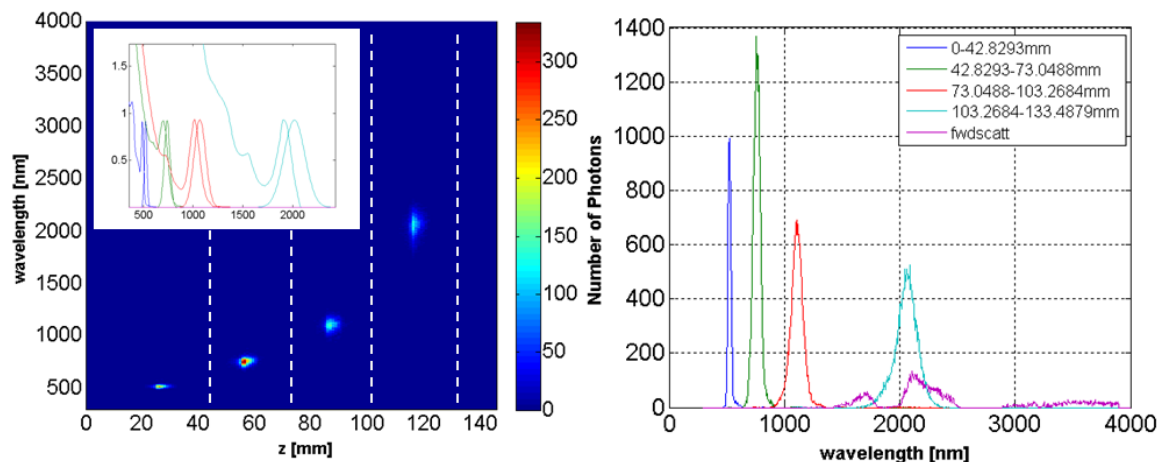
Figure 4. Two representations of the wavelength spectrum of the LSS optical output are given as a function of *z*. On the left a color map indicates number of photons emitted at each wavelength λ and position *z* out of the *N* = 100,000 input. On the right the spectrum of all photons output from four separate regions of the LSS (indicated by dashed lines on the left-hand side) plus the back end of the LSS are shown. The inset to the left figure shows the absorption and emission spectra for each color segment of this design. The design parameters yielding this result are L_{seg}/R = 5.0 and n_0 = 1.60, n_1 = 1.62, P_{trans} = 0.01, L_{space}/R = 5.04.

B. Trade-off: Quantum Efficiency vs. Concentration and Temperature

Based on the design parameters for this run we compute two illustrative net concentration values, $C_{NET,1}$ and $C_{NET,2}$. The first corresponds to a case where PV would cover all locations along the length of the LLS where a photon is emitted, and is computed by equation 5, yielding 2×. The second estimate of net concentration assumes that only the length of each color segment is covered by PV and none of the spacing between color segments has PV coverage, so instead of equation 4, the deconcentration factor of the LSS is $D_2 = 2L_{seg}/R$. The net concentration ratio based on this assumption is 9.4×. In Figure 5 we show the distribution of QE and PE along the *z*-axis of the LSS and then, based on those data, how these efficiencies vary with net concentration when the fraction of PV coverage on the LSS sidewall is varied. We find that although covering only the color segment portions of the LSS (and none of the space between) can yield a higher net concentration ratio (9.4×), one pays a penalty (~10%) in QE as the curve begins to roll off. All LSS designs exhibited a trade-off between QE and net geometric concentration (PV savings) like that shown in Figure 5(b). We can generalize that a QE within about 1%–2% of the $C_{NET,1}$ is obtained for a net concentration value around half-way between $C_{NET,1}$ and $C_{NET,2}$.
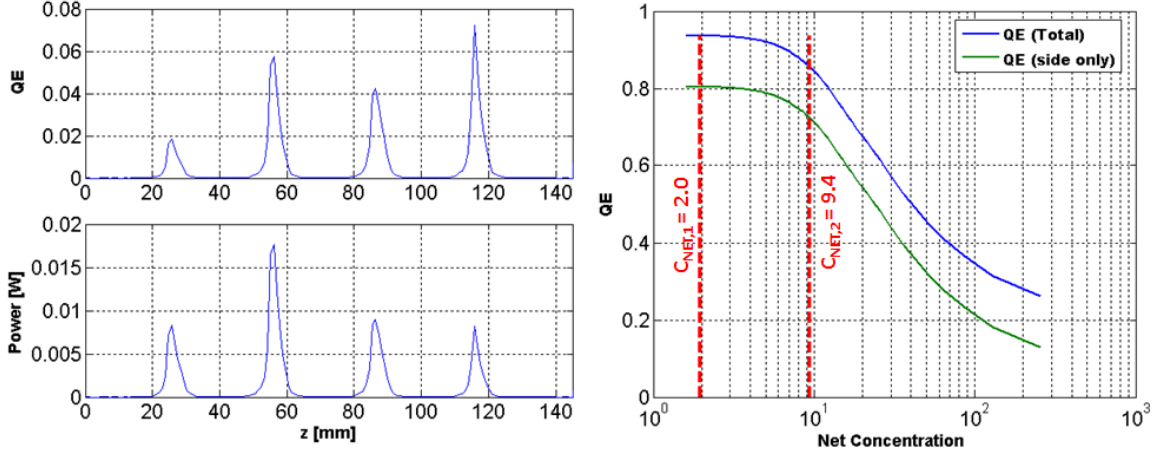
Figure 5. On the left-hand side differential quantum and power efficiency along the *z*-axis of the LSS are given for the design described in Figure 4. By sorting each differential contribution, the cumulative distribution of QE or PE can be computed as a function of cumulative length *Z* that is covered by PV. The total *Z* area that is covered is inversely proportional to net concentration of the system. The right-hand plot shows the trade-off between QE or PE and net concentration for this particular design. Red dashed lines in the plot indicate nominal concentration values: $C_{NET,2} = C_1/D_1$ where $D_1 = 2L_{seg}/R$ is computed on the basis of covering only the length of each color segment and no more; $C_{NET,1} = C_1/D_2$ where $D_2 = 2L_{seg}/R *(1 + 2 \tan\theta_{TIR})$ is based on covering not only the length of each color segment, but also the maximum *Z* distance that a ray that meets the TIR condition can traverse before meeting the wall after departing a color segment.

The previous results gave a reasonable estimate for how efficient a basic LSS design could be realized if net concentration values of less than 10× are required. We also explored how much the efficiency is reduced if much higher net concentration values are required, for example, 100×–500×. For such a case larger values of α_{LSS} are required, so n_0 must be reduced, which results in a lower fraction of isotropic emission escaping the sidewalls of the LSS and therefore lower QE. More important, though, is temperature. Because of the deconcentration factor (greater than 2×–5× in general) required to keep the average path length for exiting photons $<L>$ lower than the average absorption length ℓ, net concentrations of 100×–500× require primary concentrations of 500×–1500×. At these primary concentrations, the radiative load into the LSS may exceed 85 W/cm^2 and if QY is much less than unity (e.g., say, 20%), heating loads can be over 10 kW/cm^3, leading to temperatures well above 100 °C. At such temperatures severe mechanical degradation would be likely, as well as the degradation of luminescent quantum yield that sets in at even moderate temperatures (e.g., 70–100 °C). For these reasons results of designs for medium and high concentration are not reported here.

C. Solar-to-Electric Conversion Estimates

We calculated the solar-to-electric conversion efficiency that would be achievable if PV cells with bandgaps matched to these optical spectra (e.g., AlInGaP, InGaAs, Si, and Ge) were coupled each of our LSS designs. We used reported V_{OC}s and EQE spectra to

compute the current generation and found that a system based on the results in Figure 4 and Figure 5 would yield a solar-to-electric conversion efficiency in the neighborhood of 30%, depending on exactly what band-gap values are chosen and how high the *Voc* actually is for each cell. The individual efficiencies of each channel were 58%, 56%, 30%, and 11% (high to low band gap). When we allowed EQE to go to unity for each cell, the system efficiency increased to around 35%, with individual channel efficiencies of 63%, 61%, 39%, and 15% (high to low band gap). For the color segments coupled to PV cells with band gaps above 1 eV, the individual channel efficiency results are quite consistent with the reported performance of PV cells (so-called photovoltaic power converters), which are designed to convert narrowband laser illumination to electricity [17–19]. In such devices light-to-electricity conversion is in the 50%–60% efficiency range. The individual channel efficiencies for lower band gaps in our model are lower because of higher dark currents. Appendix A gives a more detailed explanation of our estimates for solar-to-electric efficiency.

D. LSS Dependence on Luminescence Quantum-Yield and Other Design Parameters

Because the assumption of unity QY in the foregoing results represents by far the most optimistic of all parameter assumptions, it is important to know how sensitive the performance is to the QY of individual fluorophores. Figure 6 shows that the overall efficiency of the LSS varies almost linearly with QY. This behavior is significantly different than what would be observed in more common flat-panel LSCs, where the likelihood of reabsorption is much greater. Roughly speaking, we would expect the overall quantum efficiency of an LSS or LSC to vary according to $QY^{<n>}$, where $<n>$ is the average number of absorption events that occur for rays entering the system. The larger $<n>$ is, the more nonlinear the dependence on QY will be. The LSS is designed to have $<n> \approx 1$, and we see this realized in Figure 6.

We evaluated the sensitivity of LSS performance to a large number of parameters besides QY. These included (with associated range of variation): L_{seg}/R (0.01–50), n_0 (1.0–1.6), n_1 (1.5–1.62), P_{trans} (0.005–0.1), and L_{space}/R (2–50). Of these parameters, the optical efficiency was most sensitive to n_0, followed by L_{seg}/R. The dependence of total QE on P_{trans} was quite weak because it included photons that exit the back of the LSS; however, the high QE out the side of LSS requires P_{trans} to be low (less than 0.05). Another reason P_{trans} must be small is the ratio of PE/QE goes down as P_{trans} increases, since it permits a larger fraction of light that is intended to be absorbed to pass to the next segment with a lower energy bandgap. We also experimented with varying parameters that are not yet under the LSS designer's control, given current technology. We varied the Stokes shift beyond its reported value by a factor of between 50% and 150%. This yielded a small benefit in QE of the LSS, but it also compromised the power efficiency

14

(PE). The relatively limited QE benefit of artificially inflating the Stokes shift is an indication that reabsorption, by design, is a relatively minor factor in the performance of the LSS. Taken together, our results indicate that QY of the fluorophores is the single most important parameter that requires optimization to approach the LSS performance indicated by these results.
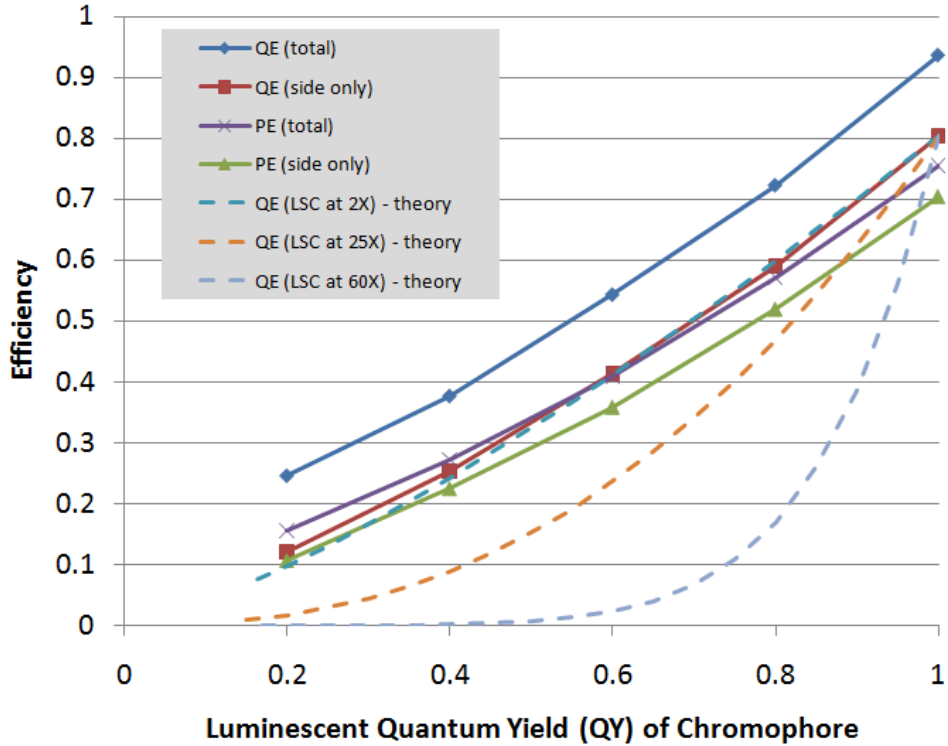
Figure 6. The dependence on fluorophore quantum yield (QY) of total QE, total PE, and side-only QE and PE (solid lines with markers) for the medium concentration LSS design whose results were given in Figure 4 and Figure 5 (L_{seg}/R = 4.0 and n_0 = 1.50, n_1 = 1.62, P_{trans} = 0.005, L_{space}/R = 15.6). For comparison, the dashed lines indicate, based on Olson et al., how LSC quantum efficiencies would scale with QY for three different geometric concentration values ranging from 2× to 60×. The average number of reabsorptions for these three LSC cases are 1.3, 4.4, and 7.0. In the calculation of theoretical LSC QE, the losses associated with isotropic emission that does not meet the TIR condition are ignored (loss cone set to zero), and values are rescaled to match the LSS at QY = 1. This emphasizes the variation of LSC QE with QY.
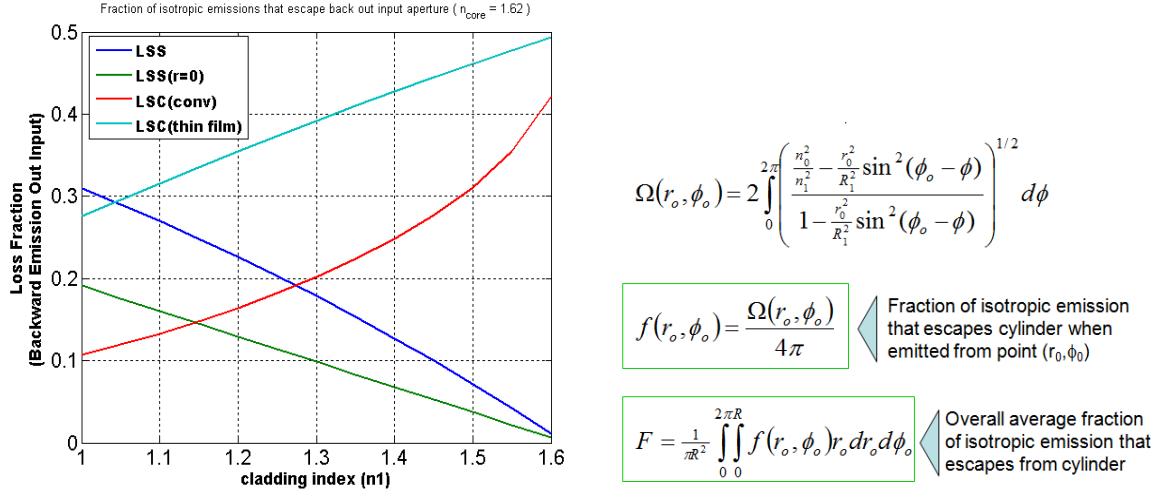
15

5. Findings

A. Loss Mechanisms in LSCs and LSS Concept

Because the LSS concept is so closely related to LSCs, it is worth comparing their main loss mechanisms. To begin with, both suffer from "return losses" incurred when a fraction of isotropically re-emitted photons (after initial absorption of the incident light) propagate back in the direction from which they originated.

For conventional LSCs, the return loss or the likelihood of isotropic emission falling within the front-side "loss cone" (i.e., not meeting the TIR criterion and propagating back out the front face) is $L_{RET,LSC} = \frac{1}{2}(1-\cos(\theta_{TIR}))$ or, in terms of the LSC and cladding refractive indices, $L_{RET,LSC} = \frac{1}{2}(1 - \sqrt{1 - (n_0/n_1)^2})$. [20, 21]. For LSCs with thin-film absorber coatings on the front exterior surface of the waveguide, emission originates from the interface between two indices. The fraction which is re-emitted back out of the front surface is given by the ensemble-averaged probability that the emission falls in the upper hemisphere with lower refractive index n_0. That probability depends on the ratio between the square of the refractive indices—the return loss probability is $n_0^2/(n_0^2 + n_1^2)$. For the case of the LSS, the return loss is a complicated expression described in Figure 9 (see Appendix B for derivation). However, the general trend can be seen in the expression for return loss along meridional rays only—emission that originates from the center of the cylinder: $L_{RET,LSS} = \frac{1}{2} \cdot (1 - \cos(\pi / 2 - \theta_{TIR})) = \frac{1}{2} \cdot (1 - n_0/n_1)$, which decreases as n_0 increases. A comparison of the return losses out the front aperture of the LSS and conventional LSC shows that they trend in opposite directions with cladding index n_0. Furthermore, we find that that for a waveguide index of $n_1 = 1.62$, the LSS can achieve lower minimum return losses (approaching zero), whereas the minimum LSC return loss is ~10% as illustrated in Figure 7, since the cladding index cannot be lower than 1. To combat the return loss in the LSS, the cladding index n_0 can be increased, but only at the expense of reducing the aperture of the LSS input and increasing deconcentration (equation 4). Both of these lead to reduced net concentration. For the cladding indices considered in this paper, the return losses ranged from 0.05 to 0.25—generally comparable to or smaller than the return losses experienced by a conventional LSC.

Another loss occurs in both the LSS and LSC when not all of the incident, above-bandgap photons are absorbed by a color segment—that is, when P_{trans} is too large. In both systems this loss is mitigated by increasing the fluorophore concentration, but the consequences for the LSS and LSC are different. When fluorophore concentration is increased for an LSC, the reabsorption probability is amplified substantially, since the path length over which emitted photons must traverse to reach the exit aperture of an LSC is much longer than the absorption path length for the incident photons. In the LSS

the opposite is true—the path length for emitted photons to exit the LSS is shorter than the absorption path length—so reabsorption is not severely affected by reducing initial absorption losses to near zero in the LSS. But ensuring complete absorption in the LSS while holding reabsorption probability constant amounts to lengthening a color segment—increasing L_{seg}/R. So the price paid for ensuring complete absorption in an LSS is *decreased* net concentration. Note, though, that the sensitivity of net concentration to L_{seg}/R is not as severe as it is to n_0.

Fraction of isotropic emissions that escape back out input aperture ($n_{core} = 1.62$)

$$\Omega(r_o,\phi_o) = 2\int_0^{2\pi} \left(\frac{\frac{n_0^2}{n_1^2} - \frac{r_o^2}{R_1^2}\sin^2(\phi_o-\phi)}{1-\frac{r_o^2}{R_1^2}\sin^2(\phi_o-\phi)} \right)^{1/2} d\phi$$

$$f(r_o,\phi_o) = \frac{\Omega(r_o,\phi_o)}{4\pi}$$

Fraction of isotropic emission that escapes cylinder when emitted from point (r_0,ϕ_0)

$$F = \frac{1}{\pi R^2}\int_0^{2\pi R}\int f(r_o,\phi_o)r_o dr_o d\phi_o$$

Overall average fraction of isotropic emission that escapes from cylinder

Figure 7. Calculated return losses for a conventional LSC (red), thin-film LSC (cyan), a cylindrical LSS (blue), and for the photons emitted from the center ($r = 0$) of a cylindrical LSS (green). These curves are based on analytic expressions and approximations stated in the text and Appendix B.

Finally, for a given device geometry, the single most important dictator of either LSS or LSC quantum efficiency is the quantum yield of individual fluorophores. However, as we noted earlier, whereas the quantum efficiency of an LSC depends on QY in a nonlinear degree, the QY dependence of the LSS should be approximately linear. This behavior of the LSS should permit a more graceful degradation of device performance if QY is compromised. A drop in fluorophore QY is the single largest risk to achieving the ideal performance indicated in the results of this paper.

One potential source of QY degradation for the fluorophores is elevated temperature. For semiconductor nanocrystals, this phenomenon is well known, though it may vary among materials. In most reports the temperature dependence of QY is documented for temperatures less than room temperature [22, 23]. Extrapolation from these results suggests that a decrease in QY of between 20% and 50% relative to RT would be expected when the temperature increases from 25 °C to 75 °C. We used the results of our Monte Carlo runs (difference between absorption and emission wavelengths) to estimate the heating load on the LSS as a function of position. An example, based on the design used for the run shown in Figure 4 and Figure 5, is given in Figure 8, showing the heat load for both QY = 100% and QY = 20%. Based on the

18

heating profile for the QY = 100% case in PMMA material and boundary conditions of constant heat-transfer coefficient on the side walls (h = 20 W/m^2/K), we use a finite element analysis (FEA) to computed temperatures ranging from 61 °C to 83 °C. The spread of temperatures occurs because the incident light absorption is exponentially distributed along the length of an LSS color section. A more sophisticated LSS design could narrow this distribution of temperatures (to about 70 °C) by varying the doping level along the length of the LSS so that the heating load is more evenly distributed along the LSS length. This result confirms that this LSS design could be operated without active cooling without too severe a temperature increase. Of course, as the temperature increases the QY can decrease, which would, in turn, feed back by increasing the heat load as more fluorophores dissipate photon excitation energy by non-radiative relaxation. Quantitative estimates of performance would require iteration between (1) FEA to determine temperature based on heating and (2) calculating QY = $f(T)$ to determine heating as function of temperature. Such an analysis was beyond the scope of this effort, but the potential for such a vicious cycle makes clear how crucial the effective removal of heat would be to the realization of any LSS design. To give a sense of how much extra heating might be observed, we also ran the FEA model using the heating load for the QY = 20% case and found average temperatures around 97 °C.
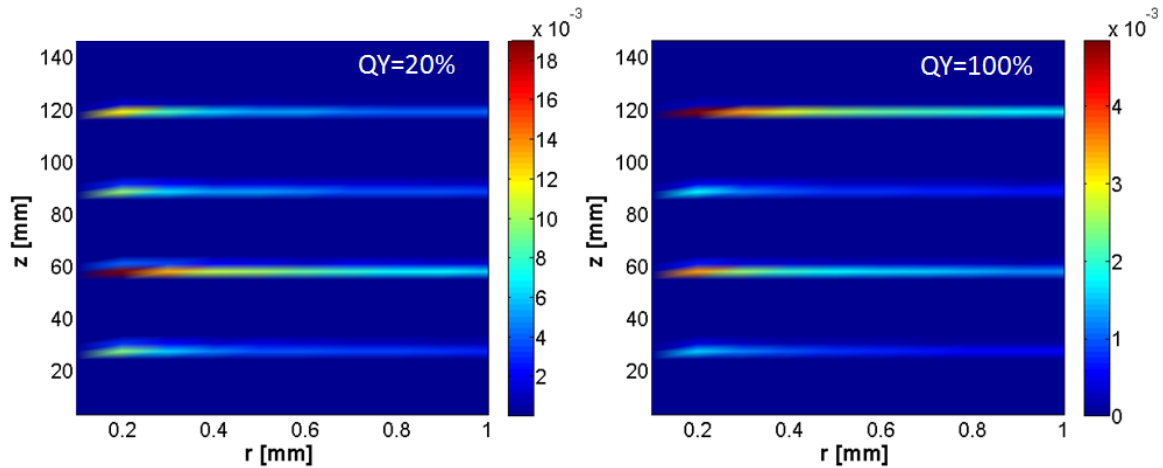
Figure 8. This plot illustrates the calculated heating loads (W/mm^3) on an LSS as a function of position along the length of the LSS and radial position inside the LSS. The heating loads are rotationally symmetric, so each coordinate on these plots gives the heating load on an annular region. The results on the right include only heating contributions arising from the energy difference between absorbed and emitted photons that arise from thermalization of photogenerated carriers to the band edge of the nanocrystal plus the Stokes shift of luminescence. It does not include heating from non-radiative relaxation since QY was unity in this model run. The heating load on the left side corresponds to the same design but with QY = 20% instead of unity, so nonradiative relaxation is included. These two cases approximate the bounds on heating inside this LSS design (minimum on left, maximum on right).

B. Overcoming the Trade-off between Quantum Efficiency and Net Concentration

The LSS results we have presented indicate that the highest optical efficiencies (and lowest operating temperatures) generally require the LSS to introduce a net *de-*concentration of the optical flux for two reasons:

1. The cladding index n_0 must be made close to n_1 to permit a large range of angles to escape the LSS. Bringing n_0 close to n_1 also reduces the numerical aperture that the LSS light guide can accommodate, which limits primary concentration and therefore temperature.
2. L_{seg}/R should be made large to reduce the probability of reabsorption for a given value of P_{trans}. Increasing L_{seg}/R also helps manage temperature by spreading the heating over a larger volume.

Through many iterations of parameter variation in our model we have found that the requirement for large n_0 drives the trade-off between concentration and QE most strongly because it affects the net concentration in two ways: (1) emitted photons are spread over a larger range of z along the LSS, and (2) larger n_0 reduces the permitted primary concentration by reducing the numerical aperture of the LSS. It is worth considering how this tradeoff might be overcome.

One option for overcoming the tradeoff between concentration and LSS efficiency that is possible with existing technology is to introduce secondary concentrator optics to the LSS that collect the optical output of the LSS and refocus it to the PV targets. No new technology is required, but a few optical limitations have to be considered. First, if we wish to employ secondary concentrators, a rectilinear LSS design would probably be preferable to the rotationally symmetric cylindrical ones considered in this paper. The more important optical constraint, however, is the fairly wide angle distribution of the optical output from the LSS. Nonimaging optics dictate that the maximum concentration an optic can deliver is related to the square of the ratio $\sin(\theta_{out}) / \sin(\theta_{in})$, where θ_{out} and θ_{in} are the maximum angles accommodated by the input and output apertures of the secondary concentrator. Figure 9 shows the angle distribution of the LSS output, which spans almost the full range of 0 to $\pi/2$, although the majority of the rays are grouped around $\pi/4$. To obtain appreciable secondary concentration, θ_{in} cannot be too large, so an optimized design might have to sacrifice some of this distribution and hence reduce its QE. Note, however, that that those rays that the secondary concentrator "rejects" would be returned to the LSS, and some of them might enjoy a second opportunity for collection in another segment. More detailed analysis would be required to identify the optimal tradeoff of ray rejection and concentration for an LSS. This idea of secondary concentration was suggested over 30 years ago for LSCs and is reported to yield between 1.5× and 2× with its limit set by the distribution of angles at the output [24, 25].

A more exotic option for overcoming the tradeoff between concentration and LSS efficiency involves a technology that does not yet exist in such a mature form: anisotropic fluorescence from aligned dipoles. Recall that the widely applied assumption of isotropic fluorescence in LSCs (and luminescent materials in general) is actually based on an ensemble average over many *anisotropic* dipoles whose orientations are randomly distributed. If the dipoles could be oriented such that they all were parallel to the z-axis of the LSS, then re-emitted photons would be more likely to propagate in a direction perpendicular to the z-axis (likely to exit the LSS) than parallel to it (trapped inside the LSS). More precisely, the probability of a photon being re-emitted with an angle θ_e relative to the z-axis would be $2 \sin^2(\theta_e) / \pi$. This kind of control over the direction of fluorescence would permit n_0 to be reduced relative to n_1 (and concentration increased), while maintaining a constant value of QE. Also, the benefit of a secondary concentrator would be enhanced since the distribution of angles for photons exiting would be smaller. On the other hand, an ensemble of uniformly aligned dipole emitters would also have enhanced absorption along the same axes as the enhanced emission (perpendicular to the z-axis). Therefore, larger values of L_{seg}/R would be required to keep the ratio between probability of reabsorption and probability of initial absorption in a color segment sufficiently low. Because n_0 drives the tradeoff between QE and net concentration more strongly than L_{seg}/R, we expect that the benefits of uniformly oriented, non-isotropic emitters to reducing n_0 would more than outweigh any required increase of L_{seg}/R to maintain low re-absorption. The feasibility of orienting dye molecules and nanocrystals at the nanoscale has been demonstrated for the purpose of improving LSC performance, among other applications [26–29]. Future investigation of LSS designs should explore this trade space using non-isotropic emission from fluorophores. If substantial benefits to LSS performance were found, it would provide a strong motivation to explore technical approaches to realizing such emitters.
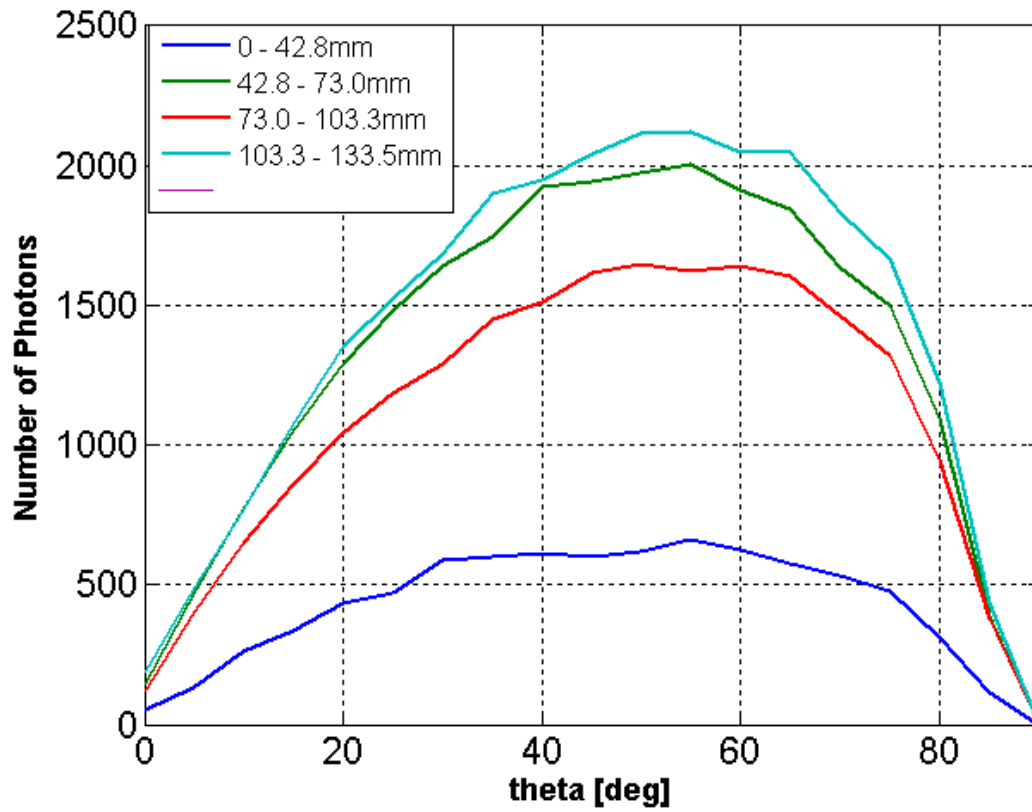
Figure 9. This plot shows the distribution of exit angles relative to the cylinder surface for rays in each segment of an LSS whose design is the same as the one for which results were given in Figure 4 and Figure 5 (medium concentration, $C_{NET,1} = 2$, $C_{NET,2} = 10$).

6. Conclusions and Summary

This paper has summarized an investigation of the performance of the LSS concept: a novel variation on LSCs for the purpose of dividing the solar (or any broadband spectrum) into spectral components with high quantum efficiency. Whereas the primary motivation of LSCs is to concentrate solar radiation, leaving division of the spectrum a secondary priority, the idea behind LSS is to design a chromophore-doped optical light guide whose *primary* function is to divide the solar spectrum, leaving concentration to other optical components in the system. Using a Monte Carlo ray-tracing model we conducted an initial exploration of the LSS design space, trying to estimate its performance limits. We found that the optical quantum efficiency and power efficiency of a cylindrical LSS can be much higher than those realized for typical LSCs, but this comes at the expense of optical concentration. We identified a notional design with net concentration between 2× and 10× whose QE reaches 95%. For designs that would permit high concentration (e.g., 100×–500×), our model indicated that the QE would be substantially reduced (to around 40%). But more important, thermal loads imposed on an LSS that seeks 100×–500× concentration would drive operating temperatures well into the 100 °C and higher. Based on this, we conclude that the LSS approach appears uniquely suited to low-concentration applications; this limits PV material options to those whose costs are not overwhelming. The QE and optical and electrical power efficiency results of our modeling do not represent true upper bounds—just the best performers in this study—so more variation of parameters including the bandgap set may yield slightly better efficiencies.

The LSS performance modeling given by the results in this paper is an idealization, but only in one major respect—the assumption of unity QY for all of the fluorophores. All other modeling assumptions, including absorption and emission spectra, were derived from existing materials and technology. Like LSCs, the performance of the LSS does critically depend on QY. However, we showed that LSS efficiency varies linearly with QY, whereas an LSC would exhibit much more sensitive nonlinear dependence on QY because the LSS requires far fewer reasborption events than an LSC before the ray exits the device. The present state of the art in nanocrystal synthesis has demonstrated luminescent QY of over 70% for CdTe, over 80% and approaching unity (>99%) for CdSe [30–33], over 80% for PbSe [34], and 50% for InAs [35], so our assumption of 100% QY to explore the potential of an LSS is optimistic, but not gratuitous. Furthermore, incorporation of nanocrystals into polymer solids has been demonstrated for many matrices, ranging from polymers to sol-gel titania matrices [10–15]. Incorporation into some matrices (particularly when a free-radical polymer initiator like AIBN is involved) can reduce the luminescent QY somewhat, but incorporation into other polymers has been demonstrated to be possible with no loss in QY [9]. Nanocrystal-

doped polymers and glasses with 100% quantum yield have not yet been realized, though there is no fundamental reason that very high QY and matrix incorporation could not be combined.

Thermal management in this approach is a central issue of which we only scratched the surface. Our preliminary thermal analysis suggested that temperatures inside an LSS under 94× primary concentration (2×–10× net concentration) would not be too severe ($T_{max} \approx$ 61–83 °C at high QY), but there remains a risk that elevated temperatures could reduce the QY. Given the interdependence of QY and temperature inside an LSS, a more detailed thermal analysis is still needed to better elucidate how a real system might perform.

We identified two design improvements that might allow the tradeoff we observed between LSS efficiency and net concentration to be broken. One, the use of secondary concentrators, probably has limitations because of the wide distribution of angles in the light that exits the LSS, but it requires no fundamental technology. The second, aligned anisotropic luminescence, represents an approach that would require significant technological development. Besides these two ideas there is definitely room for improvement of the light-pipe optical design. Recent advances in solid-state lighting optics might be brought to bear by considering, for example, non-rotationally symmetric designs. Light guides with hexagonal or rectangular cross sections, instead of circular (like the LSS considered in this study) are not only needed to accommodate flat solar cells, but also would permit tiling of multiple units into an array. Most important, though, non-rotationally symmetric designs may relax the trade-off between cladding and concentration, allowing higher concentration and improved optical efficiency. Taken together all these approaches could open a path to appreciable concentration levels that may permit the use of higher cost III-V materials that are currently available for multijunction PV.

In its present, rudimentary form, we were not able to identify LSS designs with more than low optical concentration whose ideal quantum efficiencies were high enough to promise system efficiencies (30%–40% SPE) that can outperform emerging multijunction PV cells that deliver over 40% efficiency at high concentration. However, the LSS concept demonstrates some novel points. First, simple modification of the LSC geometry can yield substantially higher QE and changes the design problem. Second, if optical spectrum splitting is the goal of a CPV module, the LSS approach offers a design that is inherently simple. This means it would be relatively inexpensive to manufacture and is likely to be robust. Furthermore, the approach is inherently extensible: adding more bandgaps to an existing, optimized design would require practically no redesign, and using nanocrystals as these designs do permits practically any bandgap set to be realized. These benefits, coupled with the potential for substantially better performance

than presented in this paper, make the LSS approach to optical splitting of the solar spectrum a topic worthy of further investigation.

7. Recommendations

This paper documents research that represents only an initial investigation of the potential utility of the LSS concept. We believe that follow-up research—including not only modeling but, more important, experimentation—is warranted. A few areas worthy of designation are listed here, but many others surely exist:

- Aligned dipoles and secondary concentration—The results of this paper made clear the trade-off that a simple LSS design demands between optical efficiency and concentration. But the discussion introduced two possible options that, taken separately or together, could break the trade-off to some degree. Significant research has already begun on the microscopic alignment of luminescent emitters, and this work could be extended to nanocrystals. After modeling the potential benefit of aligned emitter dipoles, a critical part of this research must include the development of fabrication methods that permit the individual molecules or dipoles to be aligned. One possiblility: extrusion methods for fabricating a waveguide could naturally drive high-aspect-ratio nanowires into some amount of alignment. Research into this area as well as others, including the potential benefit of secondary concentration for an LSS, could go a long way toward enabling higher net optical concentration without sacrificing too much efficiency.

- Low-cost PV at a variety of bandgaps, especially bandgaps above 2 eV—As the discussion section made clear, most of the PV materials that offer good performance at a variety of bandgaps between 1 eV and 2 eV are based on III-V materials that use very expensive substrates and are expensive to grow and process. Typical prices for III-V cells on Ge or GaAs substrates exceed $100,000/m^2 at present (compared with \$400–\$600/m^2 for silicon PV). At these prices, a CPV design needs to provide significant concentration to drive down the cost of III-V PV material per unit area of the finished module. The current limitations on concentration for the LSS concept preclude it from using high-performance III-V materials of this variety in any economically competitive way. However, future development of new PV materials on inexpensive substrates—or PV materials that could be fabricated directly onto the surface of a LSS—that cover a wide variety of band-gap values (especially $E_g > 2$ eV) could make the LSS approach much more commercially interesting.

- Optimizing PV for narrow-band spectra—The development of low-cost III-V (and other materials) is a goal that is practically as old as photovoltaics, but the LSS approach offers a potentially new opportunity: the PV no longer needs to efficiently convert a wide-band incident spectrum. Instead, the LSS illuminates the PV on each spectrum channel with a narrow-band spectrum. In principle,

this should make the design requirements of the PV less demanding, so a variety of cost-cutting opportunities may be found with a concerted research effort. The main two requirements of the PV design are (1) high EQE over a 50 nm bandwidth at the band edge and (2) maximum V_{OC} for the given illumination spectrum. It may be possible to achieve high performance over this much more limited spectral band for many materials without the requirements of certain window layers, confinement layers, or minimized surface recombination velocities.

- Improved light pipe design—Rectilinear, hexagonal, and other non-rotationally symmetric designs should be explored to identify designs that yield better optical efficiency and that relax the tradeoff between cladding and net optical concentration. Non-rotationally symmetric designs are needed to accommodate flat solar cells and would permit the tiling of many units into arrays. Work in this direction should leverage recent developments in the field of solid-state lighting.

- Investigate the photobleaching and QY degradation of luminescent materials— Both the immediate (short-term) QY loss associated with heating and longer term loss from photobleaching are important to quantify and understand. One of the reasons for ongoing interest in semiconductor inorganic nanocrystals is their relative resistance to photobleaching (compared with organic dyes). Under what circumstances the QY would remain robust over many years of exposure to luminescence and thermal cycling remains to be better understood.

REFERENCES

1. A. G. Imenes, D. R. Mills, "Spectral Beam Splitting Technology for Increased Conversion Efficiency in Solar Concentrating Systems: A Review," *Solar Energy Materials & Solar Cells* 84 (2004): 19–69.

2. M. A. Smith, S. Sinharoy, V. G. Weizer, O. Khan, A. Pal, E. B. Clarc, D. M. Wilt, D. A. Scheiman, N. Mardesich, "Solar Cells for NASA RAINBOW Concentrator," IEEE (2000): 1139–41.

3. C. R. Lewis, W. M. Phillips, V. B. Shields, P. M. Stella, I. Bekey, "Multi-bandgap High Efficiency Converter (RAINBOW)," *Proceedings of the Intersociety Energy Conversion Engineering Conference* 1, 401–6.

4. J. E. Ludman, J. L. Sampson, R. A. Bradbury, J. G. Martin, J. Riccobono, G. Sliker, E. Rallis, "Photovoltaic Systems Based on Spectrally Selective Holographic Concentrators," *Proceedings of SPIE* 1667 (1992): 182–9.

5. A. Barnett et al., "Very High Efficiency Solar Cell Modules," *Progress in Photovoltaics: Research and Applications* 17(1): 75–83.

6. A. Barnett, C. Honsberg, D. Kirkpatrick, S. Kurtz, D. Moore, D. Salzman, R. Schwartz, K. Emery, "50% Efficient Solar Cell Architectures and Designs," *Conference Record of the 2006 IEEE 4th World Conference on Photovoltaic Energy Conversion,* WCPEC-4 2, art. no. 4060203, 2560–64.

7. Mark McDonald, "Spectral Efficiency Scaling of Performance Ratio for Multijunction Cells," Conference Record of the IEEE Photovoltaic Specialists Conference, art. no. 5411236, 1215–20.

8. R. W. Olson, R. F., Loring M. D. Fayer, "Luminescent Solar Concentrators and the Reabsorption Problem," *Applied Optics* 20, no. 17 (1981): 2934.

9. Ylva K. Olsson, Gang Chen, Ronen Rapaport, Dan T. Fuchs, Vikram C. Sundar, Jonathan S. Steckel, Moungi G. Bawendi, Assaf Aharoni, and Uri Banin, "Fabrication and Optical Properties of Polymeric Waveguides Containing Nanocrystalline Quantum Dots," *Applied Physics Letters* 85, no. 19 (2004): 4469.

10. J. W. Lee, V. C. Sundar, J. R. Heine, M. G. Bawendi, K. F. Jensen, "Full Color Emission from II-VI Semiconductor Quantum Dot—Polymer Composites," *Advanced Materials* 12 (2000): 1102. Note: Table 1 = QY is somewhat lower than pre-polymerization.

11. J. W. Lee, "Semiconductor Nanocrystal Composite Materials and Devices," Doctoral Thesis, Massachusetts Institute of Technology, June 2002. Note, p. 114: polymer encapsulation leaves 65% of original QY.

12. W. C. Sheng S. Kim J. Lee, S. W. Kim, K. Jensen, M. G. Bawendi, "In-situ Encapsulation of Quantum Dots into Polymer Microspheres," *Langmuir* 22 (2006): 3782–90.

13. V. C. Sundar, H. J. Eisler, Y. T. Chan, E. L. Thomas, M. G. Bawendi, "Soft Lithographically Embossed Multilayered Distributed Feedback Nanocrystal Lasers," *Advanced Materials* 16, no. 23–24, 2137.

14. V. C. Sundar, H. J. Eisler, M. G. Bawendi, "Room Temperature, Tunable Gain Media from NOvel II-VI Nanocrystal-Titania Composite Matrices," *Advaned Materials* 14, no. 10 (2002): 739.

15. R. Reisfeld, "Prospects of Sol-Gel Technology Towards Luminescent Materials," *Optical Materials* 16 (1-2) (2001): 1–7.

16. R. Winston, J. C. Minano, P. Benitez, *Nonimaging Optics* (New York: Elsevier Academic Press 2005).

17. M. Ilegems, B. Schwartz, L. A. Koszi, and R. C. Miller, "Integrated Mulcijunction GaAs Photodetector with High Output Voltage," *Appl. Phys. Lett.* 33 (1978): 629–31.

18. R. C. Miller, B. Schwartz, L. A. Koszi, and W. R. Wagner, "A High-Efficiency GaAlAs Double-Heterostructure Photovoltaic Detector," *Appl. Phys. Letr.* 33 (1978): 721–23.

19. H. D. Law, W. W. Ng, K. Nakano, P. D. Dapkus, and D. R. Stone, "High Efficiency InGaAsP Photovoltaic Power Converter," *IEEE Electron Device Letters.* 2, no. 2 (1981): 26–27.

20. C. L. Mulder, P. D. Reusswig A. M. Velazquez, H. Kim, C. Rotschild, M. A. Baldo, "Dye Alignment in Luminescent Solar Concentrators: I. Vertical Alignment for Improved Wavefuid Coupling," *Optics Express* 18, no. S1 (2010): A79.

21. S. A. Evenson, A. H. Rawicz, "Thin-Film Luminescent Concentrators for Integrated Devices," *Applied Optics* 34, no. 31 (1995): 7231.

22. G. W. Walker, V. C. Sundar, C. M. Rudzinski, A. W. Wun, M. G. Bawendi, D. G. Nocera, "Quantum-Dot Optical Temperature Probes," *Applied Physics Letters* 83, no. 17 (2003): 3555.

23. B. F. Fisher, "Time Resolved Fluorescence of CdSe Nanocrystals Using Single Molecule Spectroscopy," Ph.D. dissertation, Massachusetts Institute of Technology, 2005, 117.

24. A. Goetzberger, "Fluorescent Solar Energy Concentrators: Principle and Present-State-of-Development," *2009 Springer Series in Optical Sciences*, 159.

25. A. Goetzberger, O. Schirmer, *Appl. Phys.* 19 (1979): 53.

26. R. V. Talroze, G. A. Shandryuk, A. S. Merekalov, A. M. Shatalova, O. A. Otmakhova, "Alignmnet of Nanoparticles in Polymer Matrices," *Polymer Science, Series A* 51, no. 11 (2009): 1930–39.

27. M. G. Debije, D. J. Broer, and C. W. M. Bastiansen, "Effect of Dye Alignment on the Output of a Luminescent Solar Concentrator," Presented at the 22nd European Photovoltaics Solar Energy Conference, Milan, Italy, 3–7, September 2007.

28. C.L. Mulder, P. D. Reusswig, A. M. Velázquez, H. Kim, C. Rotschild, M. A. Baldo, "Dye Alignment in Luminescent Solar Concentrators: I. Vertical Alignment for Improved Waveguide Coupling," *Optics Express*, 51, no. S1 (2010): A79.

29. C. L. Mulder, P. D. Reusswig, A. P. Beyler, H. Kim, C. Rotschild, M. A. Baldo, "Dye Alignment in Luminescent Solar Concentrators: II. Horizontal Alignment for Energy Harvesting in Linear Polarizers," *Optics Express*, 18, no. S1 (2010): A91.

30. J. Mcbride, J. Treadway, L. C. Feldman, S. J. Pennycook, S.J. Rosenthal, "Structural Basis for Near Unity Quantum Yield Core/Shell Nanostructures," *Nano Letters* 6, Issue 7 (July 2006): 1496–1501.

31. Peng, X., Schlamp, M.C., Kadavanich, A.V., Alivisatos, A.P., Epitaxial Growth of Highly Luminescent CdSe/CdS Core/Shell Nanocrystals with Photostability and Electronic Accessibility, *Journal of the American Chemical Society* 119, Issue 30 (July 1997): 7019–7029.

32. Peter Reissa, Sophie Carayon, Joel Bleuse, "Large Fuorescence Quantum Yield and Low Size Dispersion from CdSe/ZnSe Core/Shell Nanocrystals," *Physica E* 17 (2003): 95.

33. Markus Grabolle, Monika Spieles, Vladimir Lesnyak, Nikolai Gaponik, Alexander Eychmüller, and Ute Resch-Genger, "Determination of the Fluorescence Quantum Yield of Quantum Dots: Suitable Procedures and Achievable Uncertainties," *Analytical Chemistry* 81 (2009): 6285.

34. Brian L. Wehrenberg, Congjun Wang, and Philippe Guyot-Sionnest, "Interband and Intraband Optical Studies of PbSe Colloidal Quantum Dots," *J. Phys. Chem. B* 106 (2002): 10634–40.

35. Peter M. Allen, Wenhao Liu, Vikash P. Chauhan, Jungmin Lee, Alice Y. Ting, Dai Fukumura, Rakesh K. Jain, and Moungi G. Bawendi, "InAs(ZnCdS) Quantum Dots Optimized for Biological Imaging in the Near-Infrared," *J. Am. Chem. Soc.* 132 (2010): 470–71.

Appendix A—Supplementary 1: Solar-to-Electric System Efficiency Model

This section describes how we computed estimates of the electrical power output of PV cells coupled to an LSS under AM1.5D illumination. Experimental data from actual PV cells formed the basis of these estimates so that they would be consistent with existing technology. The general approach can be summarized as: (1) obtain EQE spectrum for each PV cell; (2) compute the optical power spectrum of the LSS output; (3) match the LSS output spectrum to the corresponding EQE spectrum to obtain the short-circuit current of each cell, Isc; (4) compute the open-circuit voltage of each cell, Voc, based on either Isc or by extrapolation from experimentally reported Voc values; (4) compute fill factor FF, based on Voc for each cell; (5) compute power output of each cell as the product of Isc, *Voc*, and FF.

The nanocrystal band edges (luminescence) used in the LSS results of this paper were 489 nm, 695 nm, 1010 nm, and 1900 nm. Based on the luminescent output of the LSS, we selected the following set of desired bandgaps for the PV that we might couple to the LSS: 2.1 eV, 1.45 eV, 0.99 eV, 0.56 eV. We were not able to identify literature reports for PV with these exact bandgaps. Instead, we identified a set of eight different reports on PV cells that were generally made of ternary or quaternary III-V semiconductor materials. This meant that the results which were reported on each PV cell at a particular bandgap can plausibly be shifted within a certain range to match the bandgaps we desire. The experimental EQE for eight different PV cells that we identified are given in Figure 10. Table 1 lists the material to which each of the EQE spectra corresponds, as well as a more general material class of which that material is a member. For each of the eight types of material, we identified a range of bandgaps over which such a material might reasonably be tuned. We then used these as a look-up table for assigning EQE spectra to each PV cell in our solar-to-electric conversion model. As an example, consider the third color segment of our notional LSS for which we identified PV with a band gap of 0.99 eV as suitable. We approximate a realistic EQE for our notional cell by the following steps. First, identify InGaAs as the material into whose bandgap domain 0.99 eV falls. Then take the representative example of this material—a 0.89 eV InGaAs cell—and translate its EQE spectrum (cyan line in Figure 10) by the difference between its actual bandgap and our desired bandgap, 0.99 − 0.89 = 0.1 eV, to obtain the experimental EQE spectrum of the notional PV cell placed on the third segment of this LSS design. The result of carrying out this procedure for all five output channels of the LSS is overlaid on a rescaled power spectrum of the LSS output in Figure 11.
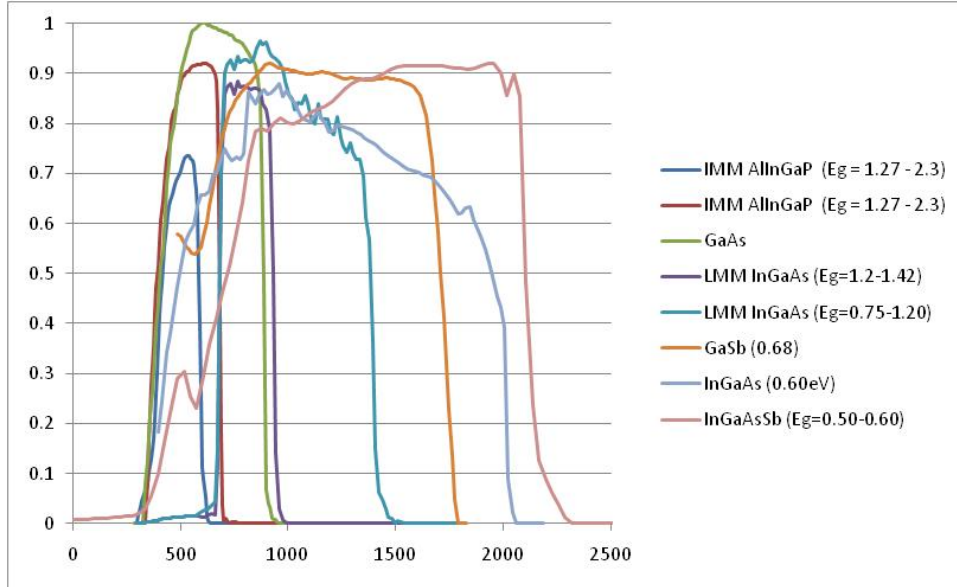
Figure 10. EQE Spectra from reports on eight different PV cells of various materials and band gaps.

Table 1. List of the eight different PV materials whose experimental EQE are given in Figure 10, along with a more general material class to which each material belongs and over which its band gap could be tuned.

SELECTED LABORATORY CELLS	GENERIC CELL CLASS	Bandgap Range: MIN	Bandgap Range: MAX
LMM InGaP (2.1eV)	IMM AlInGaP (Eg = 1.27 - 2.3)	2.1	2.35
LM InGaP (1.83eV)	IMM AlInGaP (Eg = 1.27 - 2.3)	1.43	2.1
GaAs (crystalline)	GaAs	1.42	1.43
IMM InGaAs (1.34eV; In=4%)	LMM InGaAs (Eg=1.2-1.42)	1.2	1.42
IMM InGaAs (0.89eV; In=37%) + IM	LMM InGaAs (Eg=0.75-1.20)	0.75	1.2
GaSb (0.68)	GaSb	0.67	0.75
InGaAs (0.60eV)	InGaAs (Eg=0.60-0.75)	0.6	0.67
InGaAsSb (0.56eV)	InGaAsSb (Eg=0.50-0.60)	0.5	0.6

To model performance in the limit of nearly perfect EQE, we also carried out runs for which we dispensed with the experimental EQE spectra altogether, replacing them with simple Heaviside step functions that are 0 below the band gap and a constant value above the band gap. We set the constant to either the maximum value from each of the eight representative EQE spectra or to unity. Increasing the EQE to either of these ideal cases gave us a sense for how much improvement could be realized if cells with ideal EQE were coupled to the LSS system.

34
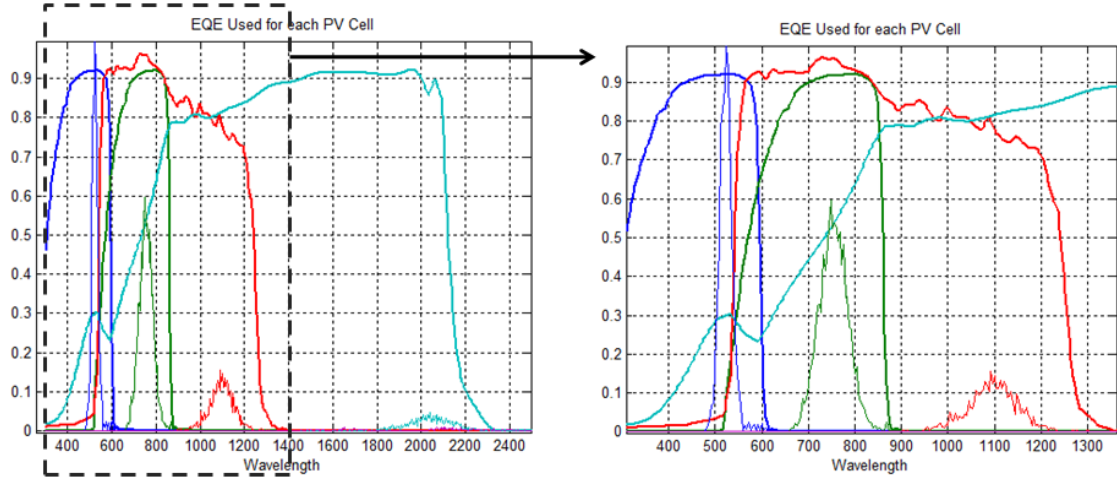
Figure 11. Modified experimental EQE spectra overlaid on a rescaled power spectrum of the optical output of the LSS described in figure 7 of the results. These EQE spectra come from measurements in real materials, but are translated a small amount to correspond to the desired band gap for the notional PV cell.

To compute the short-circuit current of each PV cell in the system model, we require not only a realistic EQE spectrum for each cell, but also an accurate estimate of the number of photons emitted from the LSS at each wavelength. The results given in Figure 4–Figure 7 tell us how many of N_{MC} input photons were emitted in the Monte Carlo simulation, but the number used for the simulation, N_{MC}, is far smaller than the actual number of photons that would be incident on the LSS per second in actual operation. Therefore, we computed a scale factor to convert the Monte Carlo spectrum to an estimate of the actual number of photons emitter per second under real conditions. The number of photons incident on the LSS device is obtained by first dividing the AM1.5D spectrum by photon energy at each wavelength to yield a "number spectrum" of incident light per square meter per second:

$$dn_{AM15}(\lambda) = \frac{dp_{AM15}(\lambda)}{hc/\lambda}$$

where the lower case variables n and p indicate number and power per unit area. We assumed that the primary optic had no losses and provided optical concentration at the limit based on its input and output acceptance angles (equation 3), so the number spectrum for photons entering the LSS is just a multiple of the number spectrum of incident radiation,

$$dN_{\text{LSS,IN}}(\lambda) = C_{1\text{max}} \times A_{\text{LSS,IN}} \times dn_{AM15}(\lambda)$$

35

We set the input aperture of the LSS to $A_{\mathrm{LSS,IN}} = 3.14 \times 10^{-6}$ m^2 ($R = 1$ mm). Inserting this value into equation (S2) and integrating over the spectrum gives us the total number of photons introduced to the LSS per second,

$$N_{\mathrm{LSS,IN}} = \int_{\lambda=0}^{\lambda=\infty} dN_{\mathrm{LSS,IN}}(\lambda)$$

For the three values of $C_{1\mathrm{max}}$ corresponding to the results in Figure 4–Figure 7 ($C_{1\mathrm{max}} = 546$, 719, and 94), the values of $N_{\mathrm{LSS,IN}}$ are 6.8×10^{18}, 9×10^{18}, and 1.2×10^{18}. The scale factor we desire is obtained by dividing $N_{\mathrm{LSS,IN}}$ by the actual number of photons used for the Monte Carlo simulation, N_{MC}: $\chi = N_{\mathrm{LSS,IN}} / N_{MC}$. For our simulations we used scale factors of 6.8×10^{14}, 9×10^{14}, 1.2×10^{14} (for $N_{MC} = 10{,}000$).

Using this scale factor we computed an estimate for the actual number of photons emitted by the LSS channels at each wavelength per second for each channel, k:

$$dN_{\mathrm{LSS,OUT},k}(\lambda) = \chi \times dN_{\mathrm{MC,OUT},k}(\lambda)$$

and we computed the optical power spectrum of each channel,

$$dP_{\mathrm{LSS,OUT}}(\lambda) = (hc/\lambda) \times dN_{\mathrm{LSS,OUT}}(\lambda)$$

Using $dN_{\mathrm{LSS,OUT},k}$ the actual number of photons emitted by the LSS channels at each wavelength per second and the EQE spectra described earlier, we computed the short-circuit current of each cell k:

$$I_{SC,k} = \int_{\lambda=0}^{\lambda=\infty} EQE_k(\lambda) \times dN_{\mathrm{LSS,OUT},k}(\lambda)$$

We assumed that the cells in this model would cover the entire length of the LSS, so the area of these notional cells computes as $A_{\mathrm{cell}} = 2\pi R(L_{\mathrm{seg}} + L_{\mathrm{space}})$. To get the short-circuit current density J_{SC}, we divided I_{SC} by the area of each cell, recognizing that this quantity is actually just an average of the truly non-uniform J_{SC} across the surface of the cell. By these procedures we arrived at estimates for the short-circuit current of each cell.

The next step toward estimating the electric output of the PV cells is to estimate the open-circuit voltage, which we did by several methods. The first and simplest was to employ the rule of thumb that states that V_{oc} is usually about 0.4 V below the band gap. So estimate #1 is,

$$V_{OC,k}^{(1)} \equiv \frac{E_{G,k}}{q} - 0.4$$

where q is the coulomb charge. In the second approach we computed the reported ratio between V_{oc} and E_G for each of the eight representative cells reported in Table 1. We then multiplied the desired band gap for each notional cell by the empirical ratio of the representative cell that most closely matched its band gap. In other words we extrapolated the V_{OC}/E_G ratio of reported cells to our nearby desired band gaps of each cell k.

$$V_{OC,k}^{(2)} \equiv E_{G,k}\left(\frac{V_{OC,\text{reported}}}{E_{G,\text{reported}}}\right)$$

The third method of estimating V_{OC} was based on the well known solutions to the minority carrier diffusion equations, using our estimates of J_{SC} to obtain V_{OC} in the equation,

$$V_{OC,k}^{(3)} \equiv n\frac{k_B T}{q}\ln\left(\frac{J_{SC,k}+J_{o1,k}}{J_{o1,k}}\right)$$

where T is the operating temperature (K), k_B is the Boltzmann constant, n_k is the ideality factor for cell k, and $J_{o1,k}$ is the dark current of cell k, which can be expressed as,

$$J_{o1,k} = J_{00,k}\exp\left(\frac{-E_{G,k}}{k_B T}\right)$$

One benefit of the theoretical approach is that it explicitly incorporates the benefit of higher V_{OC} when cells are operated under concentration (higher J_{SC}). But the drawback of this theoretical estimate was our lack of information on the dark saturation current and ideality factors for the cells we were modeling. For this reason we generally relied on the second method of V_{OC} estimation in our results, unless otherwise noted. This meant that our estimates generally ignored any benefits the cells would realize from operation at the higher J_{SC} levels.

The last quantity calculated was the fill factor, which we computed based on the well known empirical expression,

$$FF_k = \frac{V_{OC,k} - \frac{k_B T}{q}ln\left(\frac{qV_{OC,k}}{k_B T} + 0.72\right)}{V_{OC,k} + \frac{k_B T}{q}}$$

Finally, the power output of each cell k was computed by the product of our estimates of short-circuit current, open-circuit voltage, and fill factor on each cell, $P_k = I_{SC,k} \times V_{OC,k} \times FF_k$. Simple summation over each of these cells yielded the total electric power produced from these cells, $P_{\text{tot,elec}} = \sum_{k=1}^{N_{\text{cells}}} P_k$. This, of course, means that we are ignoring the small losses associated with the power electronics required to combine electrical output from cells of different voltage. Dividing the total electrical output of the

37

LSS by the power of the AM1.5D insolation at the input aperture of the system yielded our estimates of the solar-to-electric power efficiency:

$$\eta_{\text{solar2elec}} \equiv \frac{P_{\text{tot,elec}}}{P_{AM15}(\lambda)} = \frac{\sum_{k=1}^{N_{\text{cells}}}\left(I_{SC,k}V_{OC,k}FF_k\right)}{\left(C_{1\max} \times A_{LSS,IN}\right) \times \int_{\lambda=0}^{\lambda=\infty} dp_{AM15}(\lambda)}$$

For results quoted in the main text we relied on the using the experimental EQE spectra and estimated open-circuit voltage using the second method, $V_{OC}^{(2)}$.

Appendix B—Supplementary 2: Fraction of Isotropic Light Emission That Escapes a Cylinder of High Refractive Index

In the analysis of the LSS performance a key attribute is what fraction of isotropically emitted light escapes from inside a cylinder of refractive index n_1 and cladding index of n_0. Similarly, the return losses, or the fraction of isotropic emission that is contained by TIR and propagates back toward the entrance aperture of the LSS, is also of interest. For structures with only one dimension of translational symmetry (like the LSS), computing the fraction of isotropic emission that meets the TIR condition is not as simple as for those that have two dimensions of translational symmetry (like the planar LSC), and the expressions are more complicated. In this section, we outline a derivation of the fraction of light that does not meet the TIR condition when isotropically emitted from inside a cylinder.

The first thing to note in this problem is that the fraction that meets the TIR condition depends on the location of the origin of the isotropic emission within the cylinder. Because of the rotational symmetry of the cylinder, this fraction is not dependent on the azimuth location, but it does depend on the radial location of the origin of the emission. Our goal, then is to compute what fraction of 4π Sr is subtended by rays emitted from a location (r_0, z_0), whose angle with the cylinder wall is smaller than the TIR angle. Figure 12 illustrates the key vectors involved in setting up the problem.
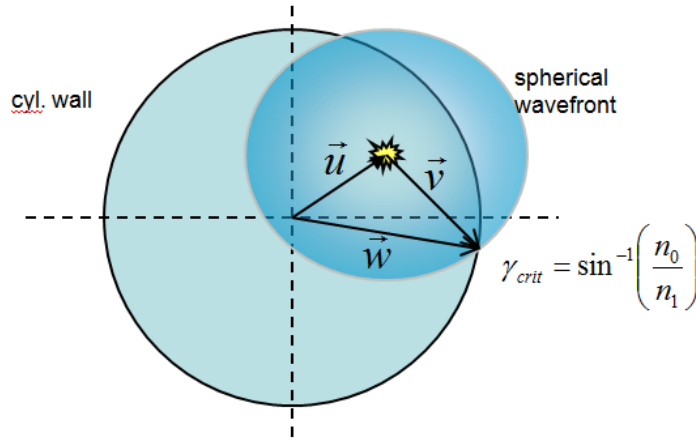
Figure 12. Illustration of vectors involved in calculation of the fraction of isotropic emission that does not meet the TIR condition.

The vector to the location of isotropic emission is $\vec{u} = \langle r_0\cos\phi_0, r_0\sin\phi_0, 0 \rangle$, and the vector of an emitted ray from the point of origin to the intersection with the cylinder wall is given by $\vec{v} = \langle \hat{\rho}\sin\hat{\theta}\cos\hat{\phi}, \hat{\rho}\sin\hat{\theta}\sin\hat{\phi}, \hat{\rho}\cos\hat{\theta} \rangle$. The position on the wall where the intersection occurs is given by the vector $\vec{w} = \langle R\cos\phi_w, R\sin\phi_w, z_w \rangle$, and the unit

normal vector of the wall at the intersection point is $\vec{n} = \langle \cos\phi_w, \sin\phi_w, 0 \rangle$, All these vectors are given in Cartesian coordinates.

The angle of incidence with the cylinder wall, γ_{AOI}, is given by the dot product of v with the normal of the cylinder wall: $\vec{v} \cdot \vec{n} = |\vec{v}||\vec{n}|\cos\gamma_{AOI} = \rho\cos\gamma_{AOI}$. Substituting the expressions for $\vec{u}$, $\vec{v}$, and $\vec{w}$ we obtain,

$$\cos\gamma_{AOI} = \sin\hat{\theta}\left(\cos\hat{\phi}\,\cos\phi_w + \sin\hat{\phi}\,\sin\phi_w\right)$$

Because we know that $\vec{w} = \vec{u} + \vec{v}$ we can obtain a system of three equations based on the three Cartesian coordinates in this equation. Using these, we compute what the spherical angles of propagation are that correspond to emission from point $\vec{u}$ and intersection at point $\vec{w}$:

$$\hat{\phi} = \tan^{-1}\left(\frac{R\sin\phi_w - r_o\sin\phi_o}{R\cos\phi_w - r_o\sin\phi_o}\right)$$

$$\hat{\theta} = \tan^{-1}\left(\frac{R\sin\phi_w - r_o\sin\phi_o}{z_w\sin\hat{\phi}}\right)$$

We substitute these angles back into the expression we computed earlier to give us the angle of incidence with the wall angle, γ_{AOI}, as a function of the origin of emission (r_o, ϕ_o) and the location on the wall (ϕ_w, z_w). The challenge now is to compute the fraction of rays from a given location $F(r_o, \phi_o)$, for which the critical angle is less than the critical angle γ_{crit}. To do this, we compute what ordered pairs $(\hat{\phi}, \hat{\theta})$ yield $\gamma_{AOI} = \gamma_{crit}$. So,

$$\cos\gamma_{AOI} = \cos\gamma_{crit} = \sin\hat{\theta}_c\left(\cos\hat{\phi}_c\cos\phi_{w,c} + \sin\hat{\phi}_c\,\sin\phi_{w,c}\right)$$

We know that $\sin\gamma_{crit} = n_0/n_1$, so $\cos\gamma_{crit} = (n_1{}^2 - n_0{}^2)^{1/2}/n_1$. Substituting this into the left hand side of previous expression and rearranging we get an expression for $\hat{\theta}_c$—the elevation angle of emission from (r_o, ϕ_o) on the azimuth ϕ_w at which the angle of intersection with the wall will be equal to the critical angle γ_{TIR}:

$$\hat{\theta}_c = \sin^{-1}\left(\frac{(n_1^2 - n_0^2)^{1/2}/n_1}{\cos\hat{\phi}_c\cos\phi_{w,c} + \sin\hat{\phi}_c\,\sin\phi_{w,c}}\right)$$

This expression is a function of (r_o, ϕ_o and ϕ_w), where $\hat{\phi}$ is given by an earlier expression. We now need an expression for ϕ_w, which is obtained by computing the intersection of the projection of the vectors $\vec{u}$, $\vec{v}$, and $\vec{w}$ in the $z = 0$ plane: $\vec{w_{z0}} = \vec{u} + \vec{v_{z0}}$ where,

$$\vec{v_{z0}} = \langle \hat{\rho}\sin\hat{\theta}\cos\hat{\phi}, \hat{\rho}\sin\hat{\theta}\sin\hat{\phi}, 0 \rangle$$

$$\vec{w_0} = \langle R\cos\phi_w, R\sin\phi_w, 0 \rangle$$

We obtain a system of two equations from the x and y components of the vector equation in the $z = 0$ plane. We solve first for the magnitude of $\overrightarrow{v_{z0}}$:

$$|\overrightarrow{v_{z0}}| = -r_o\cos(\phi_o - \hat{\phi}) \pm (r_o^2\cos^2(\phi_o - \hat{\phi}) - r_o^2 + R^2)^2$$

We can substitute this back into, for instance, the equation relating the x components of the $z = 0$ projected vectors,

$$R\cos\phi_w = r_o\cos\phi_o + |\overrightarrow{v_{z0}}|\cos\hat{\phi}$$

and rearrange to yield an expression for $\cos(\phi')$:

$$\cos\phi_w = \frac{r_o}{R}\cos\phi_o - \frac{r_o}{R}\cos\hat{\phi}\cos(\phi_o - \hat{\phi}) + \cos\hat{\phi}\left(1 - \frac{r_o^2}{R^2}\sin^2(\phi_o - \hat{\phi})\right)^{1/2}$$

When this, along with a similar expression for $\sin(\phi_w)$, is substituted back into the expression for $\hat{\theta}_c$, we obtain

$$\hat{\theta}_c = \sin^{-1}\left(\frac{(n_1^2 - n_0^2)^{1/2}/n_1}{\left(1 - \frac{r_o^2}{R^2}\sin^2(\phi_o - \hat{\phi})\right)^{1/2}}\right)$$

Which for a ray emitted at (r_o, ϕ_o) with a given azimuth $\hat{\phi}$ tells what its elevation must be to meet the TIR condition. If its elevation is less than $\hat{\theta}_c$, then the ray may exit the cylinder; if it is greater than $\hat{\theta}_c$, then it will be contained.

We next want to compute what fraction of a sphere is subtended by rays that meet the TIR condition (whose elevation is greater than $\hat{\theta}_c$). This is done by integrating over a sphere, setting the lower bound of integration on the elevation angle equal to $\hat{\theta}_c = f(\hat{\phi})$:

$$\Omega = \int_0^{2\pi} d\hat{\phi} \int_{\hat{\theta}_c}^{\pi - \hat{\theta}_c} \sin\theta \, d\theta = \int_0^{2\pi} 2\cos\hat{\theta}_c \, d\hat{\phi}$$

When we substitute the expression for $\hat{\theta}_c$ (converting from cosine to sine) and then divide by 4π steradian, we obtain the fraction of isotropic luminescence that does not meet the TIR condition and originates from (r_o, ϕ_o):

41

$$f(r_o, \phi_o) = \frac{\Omega}{4\pi} = 2\int_0^{2\pi} \left(\frac{\frac{n_0^2}{n_1^2} - \frac{r_o^2}{R^2}\sin^2(\phi_o - \hat{\phi})}{1 - \frac{r_o^2}{R^2}\sin^2(\phi_o - \hat{\phi})} \right)^{1/2} d\hat{\phi}$$

The last step to determine the *overall* fraction of isotropic luminescence inside a cylinder that does not meet the TIR condition, *F*, is to average $f(r_o, \phi_o)$ over all positions inside the cross section of the cylinder:

$$F = \frac{1}{\pi R^2} \int_0^{2\pi} \int_0^R f(r_o, \phi_o) r_o \, dr_o \, d\phi_o$$

In our work, the integration of the last two expressions is done numerically to yield the estimates for fraction of isotropic luminescence that exits the cylinder (e.g., Figure 1 and Figure 9). Bear in mind that this computation yields the fraction of rays that does not meet the TIR condition. This fraction will be larger than the fraction that actually escapes the cylinder, of course, because that rays that do not meet the TIR condition may still be reflected, based on the probabilities given by Fresnel's reflectivity equations.

$$\Omega(r_o, \phi_o) = 2\int_0^{2\pi} \left(\frac{\frac{n_0^2}{n_1^2} - \frac{r_o^2}{R_1^2}\sin^2(\phi_o - \phi)}{1 - \frac{r_o^2}{R_1^2}\sin^2(\phi_o - \phi)} \right)^{1/2} d\phi$$

$$f(r_o, \phi_o) = \frac{\Omega(r_o, \phi_o)}{4\pi}$$

Fraction of isotropic emission that escapes cylinder when emitted from point (r_0, ϕ_0)

$$F = \frac{1}{\pi R^2} \int_0^{2\pi} \int_0^R f(r_o, \phi_o) r_o \, dr_o \, d\phi_o$$

Overall average fraction of isotropic emission that escapes from cylinder

REPORT DOCUMENTATION PAGE			Form Approved OMB No. 0704-0188
Public reporting burden for this collection of information is estimated to average 1 hour per response, including the time for reviewing instructions, searching existing data sources, gathering and maintaining the data needed, and completing and reviewing this collection of information. Send comments regarding this burden estimate or any other aspect of this collection of information, including suggestions for reducing this burden to Department of Defense, Washington Headquarters Services, Directorate for Information Operations and Reports (0704-0188), 1215 Jefferson Davis Highway, Suite 1204, Arlington, VA 22202-4302. Respondents should be aware that notwithstanding any other provision of law, no person shall be subject to any penalty for failing to comply with a collection of information if it does not display a currently valid OMB control number. **PLEASE DO NOT RETURN YOUR FORM TO THE ABOVE ADDRESS.**			

1. REPORT DATE October 2010	2. REPORT TYPE Final	3. DATES COVERED *(From–To)* November 2009 – July 2010	

4. TITLE AND SUBTITLE Luminescent Spectral Splitting: Efficient Spatial Division of Solar Spectrum at Low Concentration for Multijunction Photovoltaic Modules	5a. CONTRACT NUMBER DASW01 04 C 0003
	5b. GRANT NUMBER
	5c. PROGRAM ELEMENT NUMBER
6. AUTHOR(S) Brent Fisher John Biddle	5d. PROJECT NUMBER
	5e. TASK NUMBER DA-2-2587
	5f. WORK UNIT NUMBER
7. PERFORMING ORGANIZATION NAME(S) AND ADDRESS(ES) Institute for Defense Analyses 4850 Mark Center Drive Alexandria, VA 22311-1882	8. PERFORMING ORGANIZATION REPORT NUMBER IDA Paper NS P-4659 Log: H10-000938
9. SPONSORING / MONITORING AGENCY NAME(S) AND ADDRESS(ES) Defense Advanced Research Projects Agency 3701 North Fairfax Drive Arlington, VA 22203-1714	10. SPONSOR/MONITOR'S ACRONYM(S)
	11. SPONSOR/MONITOR'S REPORT NUMBER(S)

12. DISTRIBUTION/AVAILABILITY STATEMENT

Approved for public release; distribution is unlimited. (15 October 2010)

13. SUPPLEMENTARY NOTES

14. ABSTRACT

The purpose of this study was to investigate the potential performance of a novel concept for dividing solar radiation into spectral components that separately illuminate photovoltaic (PV) cells of different bandgaps using an optical design that (1) is simple, easily manufactured, and extensible to many spectral channels, and (2) does not achieve high geometric concentration factors. The concept that we explore leverages the approach of stacked luminescent solar concentrators (LSCs) for dividing the solar spectrum using fluorophores that are tuned to different spectral bands. However, whereas multicolor LSCs must perform two functions using the same optical component—spectral division and concentration—we consider the performance of a similar design when only one demand—spectral division—is placed on it. We find that the optical quantum and power efficiencies can be quite high (QE > 90%, PE > 80%) compared to what one might intuitively expect. When we couple the light output to a simple detailed balance model of a solar cells using experimental performance parameters we find that solar-to-electric conversion could exceed 30% with four junctions, using existing PV materials. While this does not exceed what can be achieved by HCPV designs on multijunction epitaxially grown stacks, the concept presented here has the major advantage of being easily extensible to an arbitrarily large number of spectral channels. Because of this extensibility, the number of junctions in the system is limited only by the availability of PV cells with appropriate bandgaps, so significantly higher system efficiencies should be accessible without major revision to the basic design presented here.

15. SUBJECT TERMS

photovoltaics, concentrated photovoltaics (CPV), spectral splitting, luminescent solar concentrators (LSCs), quantum dots, nanocrystals, solar energy, non-imaging optics

16. SECURITY CLASSIFICATION OF:			17. LIMITATION OF ABSTRACT	18. NUMBER OF PAGES	19a. NAME OF RESPONSIBLE PERSON Dr. Stefanie Tompkins
a. REPORT Uncl.	b. ABSTRACT Uncl.	c. THIS PAGE Uncl.	SAR	45	19b. TELEPHONE NUMBER *(include area code)* 571-248-1540